

Impacts of Coastal Terrain on Warm-Sector Heavy-Rain-Producing MCSs in Southern China

MURONG ZHANG,^{a,d} KRISTEN L. RASMUSSEN,^b ZHIYONG MENG,^a AND YIPENG HUANG^c

^a Laboratory for Climate and Ocean–Atmosphere Studies, Department of Atmospheric and Oceanic Sciences, School of Physics, Peking University, Beijing, China

^b Department of Atmospheric Sciences, Colorado State University, Fort Collins, Colorado

^c Xiamen Key Laboratory of Straits Meteorology, Xiamen Meteorological Bureau, Xiamen, China

^d State Key Laboratory of Marine Environmental Science, College of Ocean and Earth Sciences, Xiamen University, Xiamen, China

(Manuscript received 18 July 2021, in final form 11 December 2021)

ABSTRACT: Warm-sector heavy rainfall in southern China refers to the heavy rainfall that occurs within a weakly forced synoptic environment under the influence of monsoonal airflows. It is usually located near the southern coast and is characterized by poor predictability and a close relationship with coastal terrain. This study investigates the impacts of coastal terrain on the initiation, organization, and heavy rainfall potential of MCSs in warm-sector heavy rainfall over southern China using quasi-idealized WRF simulations and terrain-modification experiments. Typical warm-sector heavy rainfall events were selected to produce composite environments that forced the simulations. MCSs in these events all initiated in the early morning and developed into quasi-linear convective systems along the coast with a prominent back-building process. When the small coastal terrain is removed, the maximum 12-h rainfall accumulation decreases by ~46%. The convection initiation is advanced ~2 h with the help of orographic lifting associated with flow interaction with the coastal hills in the control experiment. Moreover, the coastal terrain weakens near-surface winds and thus decreases the deep-layer vertical wind shear component perpendicular to the coast and increases the component parallel to the coast; the coastal terrain also concentrates the moisture and instability over the coastal region by weakening the boundary layer jet. These modifications lead to faster upscale growth of convection and eventually a well-organized MCS. The coastal terrain is beneficial for back-building convection and thus persistent rainfall by providing orographic lifting for new cells on the western end of the MCS, and by facilitating a stronger and more stagnant cold pool, which stimulates new cells near its rear edge.

KEYWORDS: Orographic effects; Convective storms/systems; Mesoscale processes; Rainfall

1. Introduction

Topography has a profound impact on global precipitation patterns. Early studies depicted several basic mechanisms for orography-influenced precipitation. The most direct mechanism is the upslope precipitation mechanism (Smith 1979), where the windward slope provides forced ascent for the incoming airflow and leads to enhanced condensation and precipitation. In addition, terrain can sometimes block the air mass or redirect the low-level airflow [usually when the Froude number is small (Chu and Lin 2000)] and can eventually lead to heavy precipitation (e.g., Chen and Li 1995; Yeh and Chen 2002; and references therein). For example, cold air can be blocked against the eastern slopes of the Appalachian Mountains mostly during wintertime, namely cold-air damming (Richwien 1980), which intensifies the low-level temperature gradient between the mountains and the coast and results in intense wintertime precipitation (Rackley and Knox 2016). Additionally, a strong low-level barrier jet due to the blocking of southwesterly flow by island topography was found to be responsible for heavy rainfall along the northwestern coast of Taiwan (Li and Chen 1998; Yeh and Chen 1998). Apart from the influences above, topography can also thermally alter the precipitation by providing a mountain-

plains solenoid (MPS) circulation due to differential solar heating (Wolyn and McKee 1994).

In the context of these widely accepted orographic precipitation mechanisms, there has been a recent focus on the detailed orographic influence on deep convection globally (e.g., Chu and Lin 2000; Rasmussen and Houze 2011, 2016; Houze 2012; Kumar et al. 2014; Houze et al. 2017; Zhu et al. 2017; Mulholland et al. 2018; Bai et al. 2020). In some regions of the world, complex terrain is important within the life cycle of the deep convective systems including initiation, upscale convective growth, maintenance and transition processes, and detailed physical mechanisms may vary over different latitudes, climate zones and local terrain features (Medina et al. 2010; Rasmussen and Houze 2011, 2016; Rasmussen et al. 2014). For instance, based on multiple observations during the Terrain-influenced Monsoon Rainfall Experiment (TiMREX; Lee et al. 2009), Xu et al. (2012) investigated a long-duration MCS over southwest Taiwan and found that the cold pool formed from previous precipitation can be trapped by the high terrain over Central Mountain (~2000 m) with local “cold-air damming,” which together with the onshore low-level jet (LLJ) contributed to the repeated initiation of new convection and thus persistent heavy rainfall over the offshore and coastal region. Using convection-permitting simulations, Hua et al. (2020) studied a heavy rainfall event over North China and revealed that a small horizontal scale (less than 100 km) MPS increased the low-level convergence and

Corresponding author: Zhiyong Meng, zymeng@pku.edu.cn

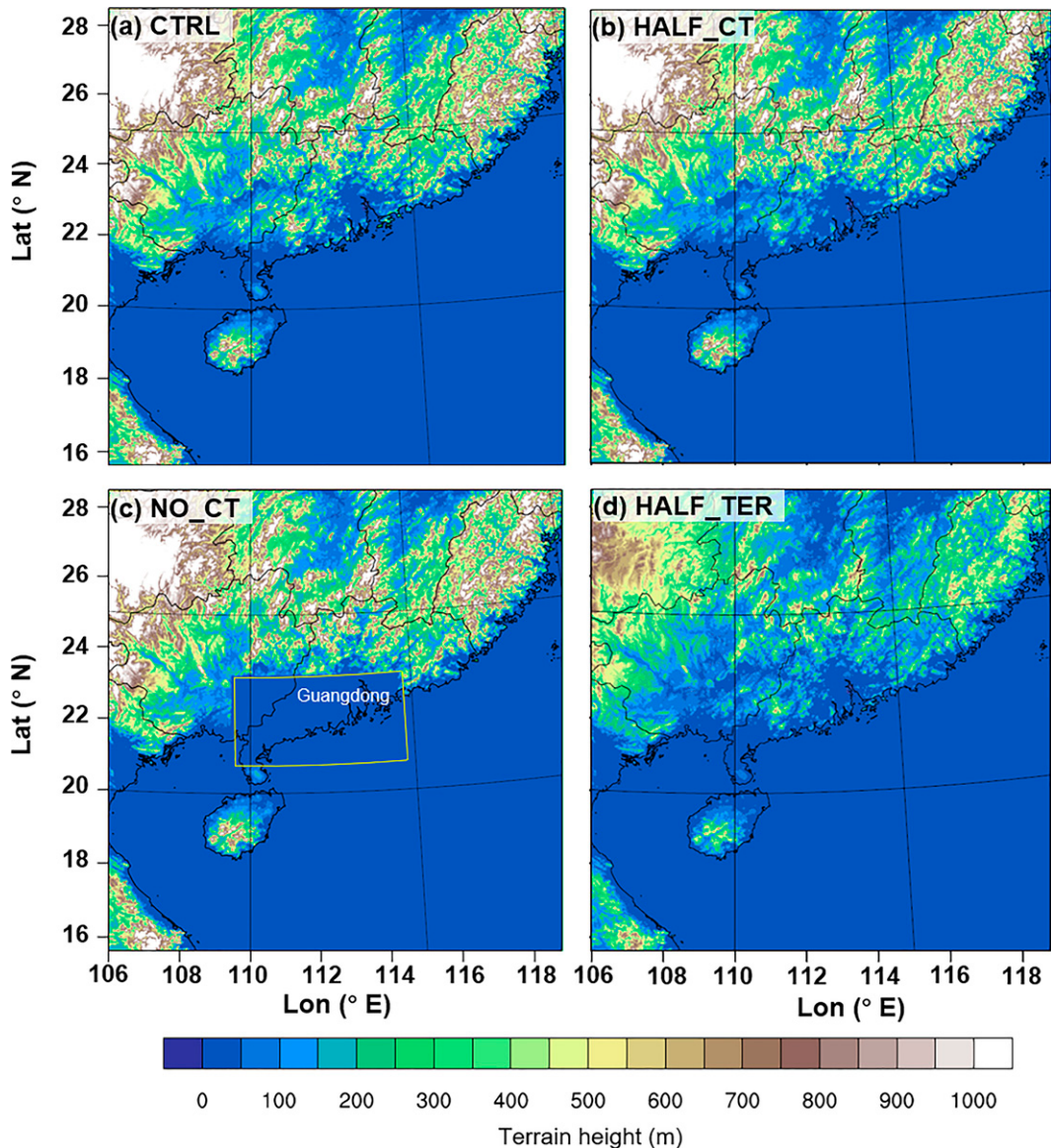


FIG. 1. WRF simulation domain (single domain) and terrain height (shading; m) in (a) CTRL, (b) HALF_CT, (c) NO_CT, and (d) HALF_TER. Guangdong Province is denoted in (c).

thus triggered the initiation of deep convection. The plateau-scale MPS was found to be responsible for the maintenance of the subsequent quasi-linear convective system by enhancing the low-level vertical wind shear that balanced the cold-pool circulation. [Mulholland et al. \(2019\)](#) focused on the terrain influence during the transition from supercell into MCSs

over the complex terrain of northern Argentina by altering the height of the Sierras de Córdoba mountains within numerical simulations. They reinforced that the terrain-induced variation in the storm environmental parameters such as vertical

TABLE 1. Selected cases for quasi-idealized WRF simulations.

	Date	Initial time (LST)	Dissipation time (LST)	Duration (h)
Case 1	26 May 2013	0400	1700	13
Case 2	9 May 2014	0300	1700	14
Case 3	17 May 2015	0400	1600	12

TABLE 2. Descriptions of terrain-modification sensitivity experiments.

Expt name	Description
CTRL	Control run of quasi-idealized simulation
HALF_CT	Reduce 50% of the coastal terrain (yellow box in Fig. 1c)
NO_CT	Remove coastal terrain
HALF_TER	Reduce 50% of the terrain over whole domain
NO_TER	Remove terrain over whole domain

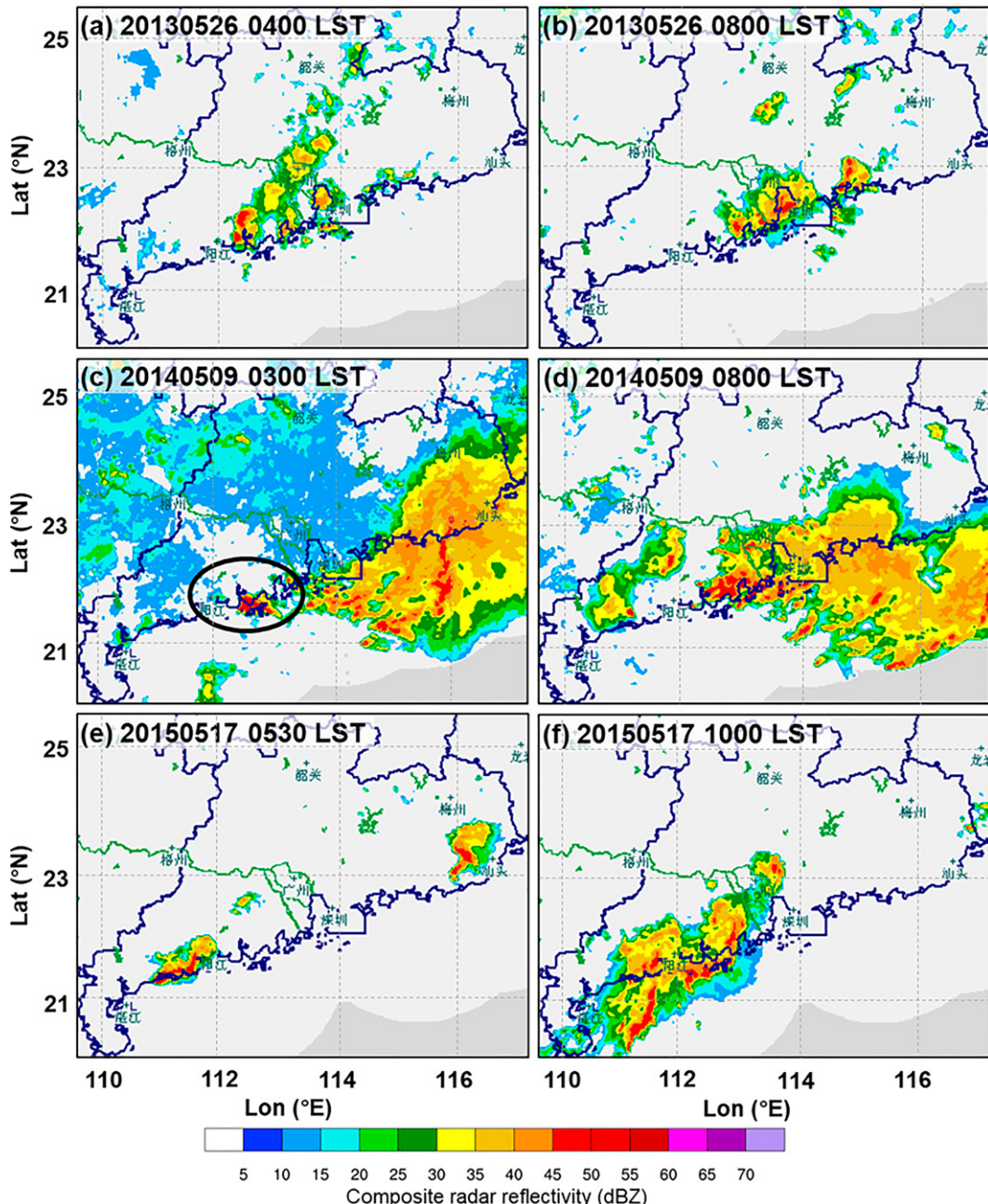


FIG. 2. Mosaics of composite radar reflectivity (shading; dBZ) over the southern coastal region in China at the (left) initial stage (early morning) and (right) mature stage (afternoon) in the three selected cases. (a),(b) Case 1 at 0400 and 0800 LST 26 May 2013; (c),(d) Case 2 at 0300 and 0800 LST 9 May 2014; and (e),(f) Case 3 at 0530 and 1000 LST 17 May 2014. The black circle in (c) denotes the MCS focused on in Case 2 in this study.

wind shear and CAPE modulated the upscale growth of the deep moist convection. Higher terrain led to a stronger vertical wind shear, which resulted in a more intense supercell that took longer to grow upscale into an MCS, while a lower terrain led to a greater mixed-layer CAPE, which resulted in a stronger and fast-moving frontal MCS that overran the focused orographic supercell and destroyed the upscale growth process.

Located in the East Asian monsoon region, southern China is one of the雨iest places in the world (Ramage 1952; Luo et al. 2020). During the pre-summer rainy season (April–June), a considerable proportion of heavy rainfall associated with MCSs occurs within a weakly forced synoptic environment, and is usually located near the southern coast under the influence of warm and moist monsoonal flow, termed warm-sector heavy rainfall (e.g., Huang 1986; Luo et al. 2013; Wang

et al. 2014; Wu and Luo 2016; Li et al. 2021). Without strong synoptic forcing, the warm-sector heavy rainfall is often characterized by lower predictability and is closely related to the low terrain near the southern coast with heights smaller than ~500 m (Fig. 1a) (Sun and Zhao 2002; Chen et al. 2016, 2017; Du and Chen 2019; Bai et al. 2021). When the low-level oceanic flow impinges on the mountainous terrain near the coast, prominent orographic effects on the rainfall intensity and life cycle of related heavy-rain-producing MCSs occur (Chu and Lin 2000; Miglietta and Rotunno 2009, 2010; Tu et al. 2019). Recently, Du et al. (2020) investigated the impacts of the terrain on a heavy-rain-producing MCS case along the southeastern coast in Guangdong based on numerical sensitivity simulations. In their case study, the coastal terrain altered the marine boundary layer jet and greatly influenced the occurrence and intensity of convection; while the local coastal concave mountain geometry was found to be able to increase coastal convergence and block the upstream moisture tongue thus fostering convection initiation (CI) and subsequent growth of initial convection. Coastal small mountains may change the location of the high frequency of CI through generating substantial local variations in the lifting and moisture pooling (Bai et al. 2021). Nevertheless, less attention has been paid on the impacts of coastal terrain in the organization of warm-sector MCSs. A more general and canonical picture of how the coastal terrain influences the initiation and organization of warm-sector heavy-rain-producing MCSs in southern China still awaits to be elucidated. The present study will answer the following questions: 1) What is the quantitative change in heavy rainfall accumulations when the coastal terrain is modified? 2) How does the coastal terrain generally modify the CI, upscale convective growth, convective evolution mode and maintenance of the heavy-rain-producing MCSs? 3) What essential dynamic and thermodynamic environmental fields are modified by the coastal terrain?

In the present study, we use convection-permitting quasi-idealized numerical simulations and terrain-modification experiments to investigate the general impacts of the coastal terrain in southern China on a warm-sector heavy-rain-producing MCS. Section 2 will introduce the data, model configurations, and sensitivity experiments settings used in this study. Section 3 will overview the three typical cases used in quasi-idealized simulations and compare the observational characteristics with the control experiment. Section 4 will reveal the response of heavy rainfall and the MCS to the changes of the coastal terrain. Section 5 will investigate the coastal terrain influence on the initiation and organization of the heavy-rain-producing MCS, respectively. Section 6 will summarize the key findings in this study.

2. Data and methods

a. Observational and analysis data

The rainfall observations used in this study were obtained from the merged and gridded precipitation dataset over China (http://data.cma.cn/data/cdcdetail/dataCode/SEVP_CLI_CHN_MERGE_CMP_PRE_HOUR_GRID_0.10.html) based

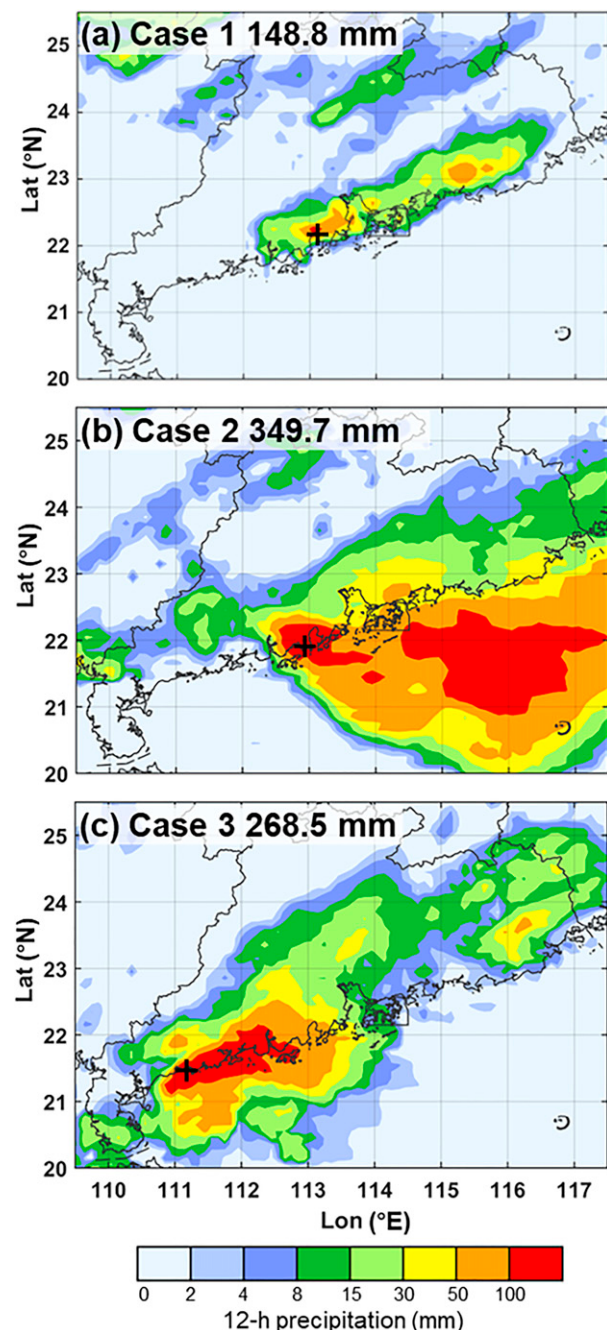


FIG. 3. The 12-h accumulated precipitation for (a) Case 1 from 0400 to 1600 LST 26 May 2013, (b) Case 2 from 0300 to 1500 LST 9 May 2014, and (c) Case 3 from 0400 to 1600 LST 17 May 2015. The maximum values of the 12-h accumulated precipitation (a) 148.8, (b) 349.7, and (c) 268.5 mm are given in the figure label and are denoted in black crosses, respectively.

on the Climate Prediction Center morphing technique (CMORPH) rainfall data (Joyce et al. 2004) and more than 30 000 automatic rain gauges over China, which provides hourly rainfall observations over 70°–140°E, 15°–60°N since 2008 with the horizontal resolution of 0.1°. The evolution of

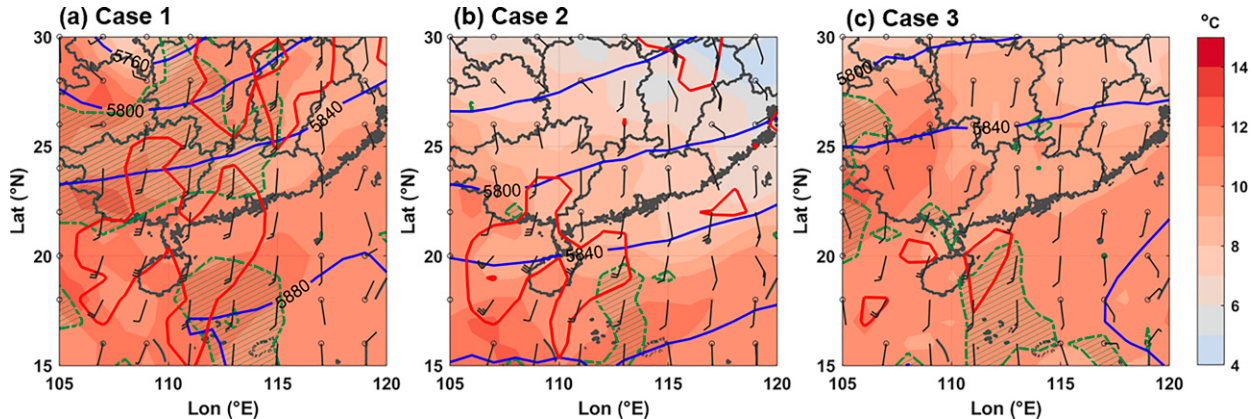


FIG. 4. Synoptic environment for the three cases at 0000 UTC (a) 26 May 2013 for Case 1, (b) 9 May 2014 for Case 2, and (c) 17 May 2015 for Case 3 revealed by FNL analysis, including 500-hPa geopotential height (contoured in blue every 40 gpm), 700-hPa temperature (shading; °C), 925-hPa specific humidity (hatched in green, over 16 g kg^{-1}), 925-hPa horizontal wind vector (full barb denotes 5 m s^{-1} , half barb denotes 2.5 m s^{-1}), and 925-hPa horizontal wind speed (contoured in red, 10 m s^{-1}).

the warm-sector heavy-rain-producing MCSs selected in this study are depicted by the mosaics of composite radar reflectivity operationally created every 6 min by the China Meteorological Administration based on a network of Chinese next-generation weather radars (S-band radars over southern China). The NCAR-archived National Centers for Environmental Prediction Final Analysis (FNL) dataset ([NCEP 2000](#)) with a horizontal grid spacing of 1° and a 6-h time interval, was used for composite analyses of the synoptic environments and the initial and boundary conditions for the quasi-idealized WRF simulations.

b. Quasi-idealized simulations and numerical model configurations

To investigate the general impacts of the coastal terrain on warm-sector heavy-rain-producing MCSs, quasi-idealized WRF simulations ([Peters and Schumacher 2015](#); [Chen et al. 2016](#)) were performed using atmospheric fields composited over observed cases as the initial and boundary conditions. The construction of the composite atmospheric fields can highlight the important role of the common features in the synoptic condition of warm-sector heavy rainfall, mitigate patterns biased by single cases, and thus lead to more general results. The frequency of warm-sector heavy rainfall events lasting more than 12 h over southern China is ~ 5 per year ([Zhang and Meng 2019](#)). Three typical warm-sector heavy rainfall events over the southern coast in China from 2013 to 2015 with similar CI timing, organization mode and duration were selected in the present study ([Table 1](#); details given in [section 3](#)). Based on the similar duration of the three events, composite FNL analysis fields with diurnal variations were obtained at 1200 and 1800 UTC Day 1 and 0000, 0600, and 1200 UTC Day 2. Considering the CI timing of the three cases was in the early morning (1900–2200 UTC, i.e., 0300–0600 LST), the composite field at 1200 UTC Day 1 was selected as the initial condition for

integration to ensure a spinup time of at least 6 h. The integration was performed for 24 h with 6-h updated composite fields serving as boundary conditions.

The control quasi-idealized simulation was performed using version 3.9.1.1 of the WRF-ARW Model ([Skamarock et al. 2008](#)). One single domain ([Fig. 1a](#)) with 51 stretched vertical levels and a 2-km horizontal grid spacing was applied. A single domain was used for quasi-idealized simulations to avoid potential errors induced by compositing the individual cases that may have larger discrepancies over larger parent domains. The quasi-idealized simulation with 2-km horizontal grid spacing accurately reproduced the typical features of convection initiation and organization of the warm-sector MCS (shown later), which met the requirements for the subsequent analyses on general mesoscale processes in the warm-sector heavy rainfall. The WRF single-moment 5-class microphysics scheme (WSM5; [Hong et al. 2004](#)), the Yonsei State University PBL scheme (YSU; [Hong et al. 2006](#)), the Dudhia shortwave ([Dudhia 1989](#)), and the Rapid Radiative Transfer Model (RRTM) longwave radiation scheme ([Mlawer et al. 1997](#)) were used while no cumulus scheme was used. Prior to deciding upon using the WRF single-moment WSM5 microphysics scheme, microphysics sensitivity experiments (not shown) were performed that included several double moment schemes. The WSM5 scheme performed the best in terms of precipitation accumulation, storm characteristics including back-building, and location, thus it was chosen for this study. In addition, the WSM5 scheme was often used in heavy rainfall simulations over the southern coastal region in China in previous studies (e.g., [Chen et al. 2016](#); [Chen et al. 2017](#)), which generally showed a good consistency with observed precipitation features. The terrain elevation data used in the simulation was from the Global Multi-resolution Terrain Elevation Data 2010 with a 30-arc-s resolution ($\sim 1 \text{ km}$).

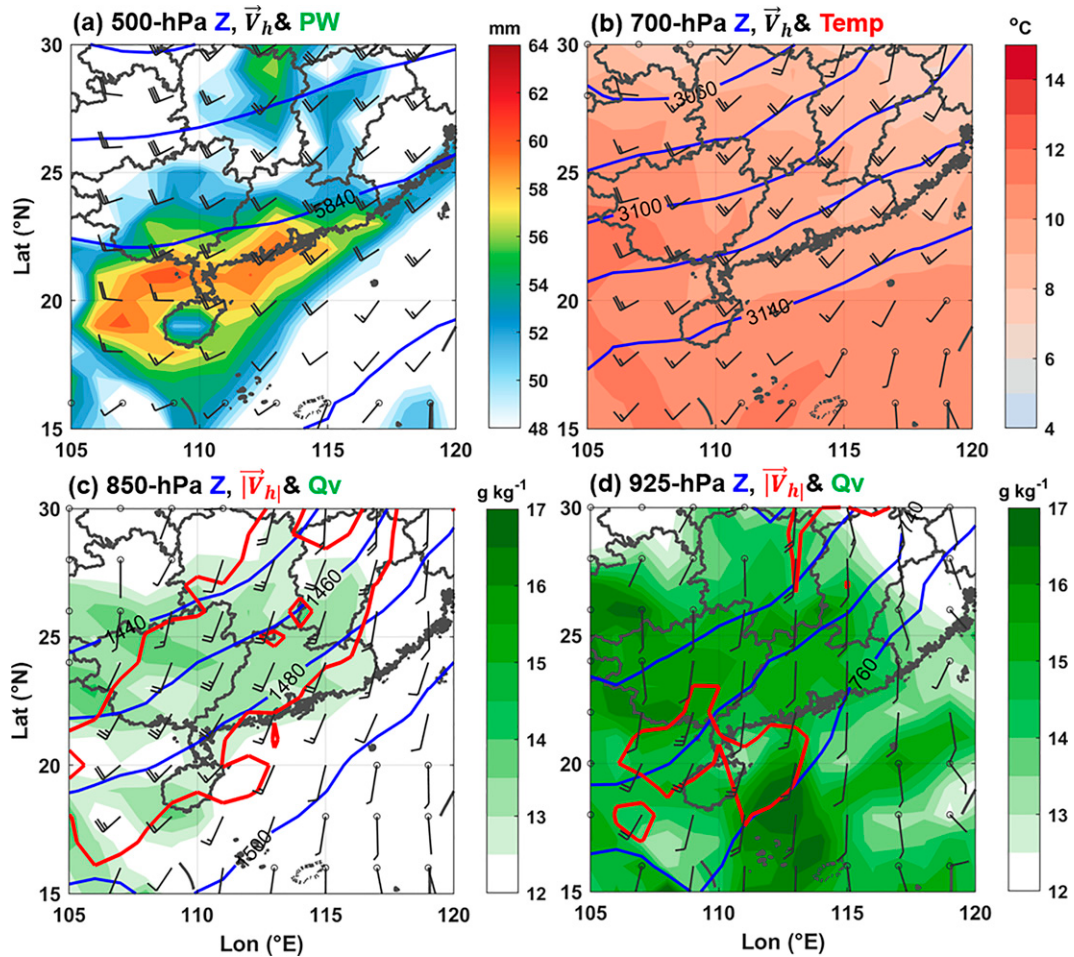


FIG. 5. Composite synoptic environment for the three cases at 0000 UTC Day 2 (averaged over 0800 LST 26 May 2013, 0800 LST 9 May 2014, and 0800 LST 17 May 2015) revealed by FNL analysis, including (a) precipitable water (shading; mm), 500-hPa geopotential height (contoured in blue every 40 gpm), and 500-hPa horizontal wind vector (full barb denotes 5 m s^{-1} , half barb denotes 2.5 m s^{-1}); (b) 700-hPa temperature (shading; $^{\circ}\text{C}$), 700-hPa geopotential height (contoured in blue every 20 gpm), and 700-hPa horizontal wind vector (full barb denotes 5 m s^{-1} , half barb denotes 2.5 m s^{-1}); (c) 850-hPa specific humidity (shading; g kg^{-1}), 850-hPa geopotential height (contoured in blue every 20 gpm), and 850-hPa horizontal wind vector (full barb denotes 5 m s^{-1} , half barb denotes 2.5 m s^{-1}) and horizontal wind speed (contoured in red, 10 m s^{-1}); and (d) as in (a), but for 925 hPa.

c. Terrain-modification sensitivity experiment design

Keeping the other model configurations the same as the control run (CTRL) mentioned above, a series of terrain-modification sensitivity experiments were designed to reveal the impacts of the coastal terrain on the convection life cycle and precipitation processes (Table 2 and Fig. 1). The terrain height modification was performed in the output files of the geogrid program in the WRF preprocessing system. Compared with CTRL, the terrain height over the coastal region in southern Guangdong Province (yellow box in Fig. 1c) was reduced by 50% in HALF_CT (with the acronym CT for coastal terrain; Fig. 1b) and fully removed in NO_CT (Fig. 1c). To compare the influence of the coastal terrain and the terrain with larger spatial range, the terrain height over the whole simulated domain was

reduced by 50% in HALF_TER (the acronym TER for terrain; Fig. 1d) and fully removed in NO_TER. To avoid the discontinuity in terrain elevation induced by the modification, a Gaussian low-pass filter of 9×9 grid cells with a standard deviation of 0.7 was applied in NO_CT and HALF_CT over both the modified region and the boundary zone with a width of 0.2° that surrounds the modified region (Figs. 1b,c). The land use types in all the sensitivity experiments remain the same as CTRL in spite of different terrain modifications.

3. Cases overview and comparison between CTRL and observations

Three warm-sector heavy rainfall events over the southern coast in China during the presummer rainy season from

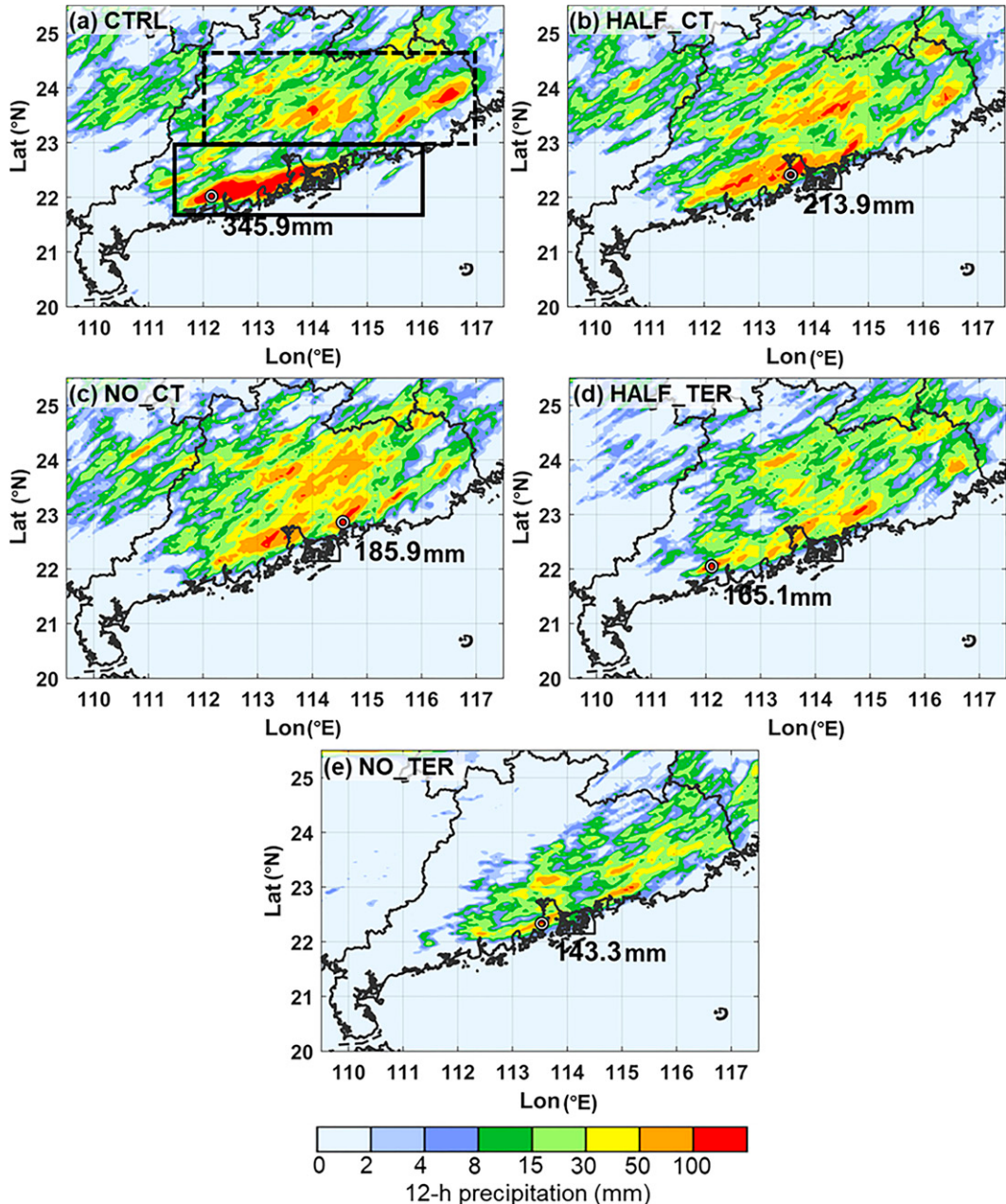


FIG. 6. The 12-h accumulated precipitation (shading; mm) from 2000 UTC Day 1 to 0800 UTC Day 2 in (a) CTRL, (b) HALF_CT, (c) NO_CT, (d) HALF_TER, and (e) NO_TER. The solid box and dashed box in (a) indicate the area used for calculating the rainfall time series (Fig. 8) over the southern coastal region (the solid box) and northern inland region (the dashed box). The small white circle denotes the location of the maximum 12-h rainfall, with the magnitude given to its lower right.

2013 to 2015 with similar MCS and precipitation characteristics were selected in this study. The CI timing here is defined as the time when the radar reflectivity first reaches 40 dBZ (following Bai et al. 2020), which is slightly stricter than the usual threshold of 35 dBZ (Roberts and Rutledge 2003; Huang et al. 2017) so that stronger initial convective cells can be identified. An MCS is defined as a continuous or quasi-continuous band of 40 dBZ reflectivity that extends

for at least 100 km in at least one direction and lasts for at least 3 h, following He et al. (2017). All of the three heavy-rain-producing MCSs initiated in the early morning (0300–0400 LST), which is near the peak time of CI of MCSs that produce warm-sector heavy rainfall in southern China according to the statistics of Li et al. (2021), and dissipated in the late afternoon (1600–1700 LST), sustaining for at least 12 h (Table 1). The initial convective cells in all of

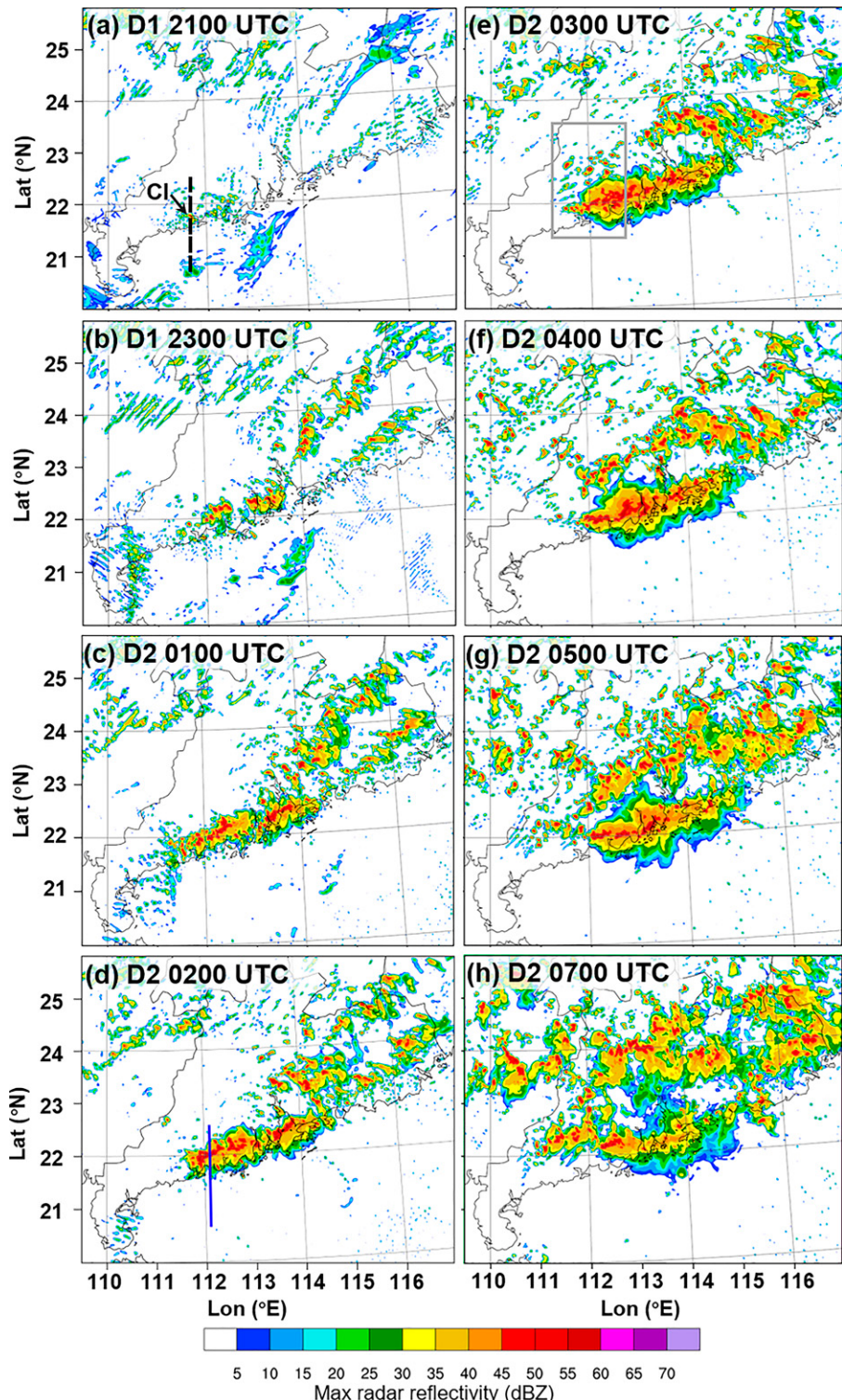


FIG. 7. Simulated maximum radar reflectivity (shading; dBZ) in CTRL at (a) 2100 UTC Day 1, (b) 2300 UTC Day 1, (c) 0100 UTC Day 2, (d) 0200 UTC Day 2, (e) 0300 UTC Day 2, (f) 0400 UTC Day 2, (g) 0500 UTC Day 2, and (h) 0700 UTC Day 2. The black dashed line in (a) gives the path for the vertical cross section in Fig. 12. The blue line in (d) gives the path for the vertical cross sections in Figs. 15 and 16. The gray box in (e) gives the region based on which the time–distance diagram is calculated in Fig. 10. The black arrow in (a) gives the location of CI.

the three cases emerged near the southern coast in Guangdong Province (hereafter Guangdong for short) (Figs. 2a,c,e), and gradually developed into a larger-scale quasi-linear convective system along the coast in 3–4 h, propagating eastward slowly. In the mature stage of each MCS, there was prominent back-building of newly generated cells on the west flank (Figs. 2b,d,f). The stratiform precipitation was mainly located to the north of the convective rainband. It is necessary to note that the MCS considered in Case 2 was the one that initiated at ~0300 LST 9 May 2014 (black circle in Fig. 2c) and merged with the previous convection downstream at ~0800 LST 9 May 2014 (Fig. 2d). The 12-h accumulated rainfall was mainly concentrated in the coastal region. The back-building processes were vital for the large rainfall accumulation on the western end of the MCS, with maximum 12-h accumulated precipitation of 148.8, 349.7, and 268.5 mm in the three cases, respectively (Fig. 3).

The synoptic conditions in the three events were generally similar and typical for warm-sector heavy rainfall. There were noticeable differences including small variations in the locations of the subtropical high, differences in moisture and temperature over the northern inland region, and differences in the strength of low-level winds among the three cases (Fig. 4). Nevertheless, each of the three cases featured 500-hPa westerlies over southern China with minimal shortwave perturbations, predominantly warm and moist southwesterly (850 hPa) and southerly (925 hPa) monsoonal flow from the upstream ocean providing abundant moisture and warm advection, and two significant BLJ cores over the northern South China Sea and Beibu Gulf. These similarities were also successfully captured by the composite fields of the three cases (Fig. 5). Notably, the LLJ patterns in the composite field (Figs. 5c,d) were identical to the general features of LLJs in warm-sector heavy rainfall events summarized in Zhang and Meng (2019), implying that the current composite fields could well represent the general synoptic conditions for warm-sector heavy rainfall.

The control simulation successfully reproduced the coastal heavy rainfall and associated MCS development. The simulated heavy rainfall distribution was mainly concentrated in the southern coastal region in Guangdong, with the maximum 12-h accumulated rainfall of 345.9 mm located at the western end of the MCS (Fig. 6a). In addition, there was widespread precipitation over the northern inland region with weaker rainfall intensity (Fig. 6a). The initial convective cells first appeared at ~111.5°E over the coastal region at 2100 UTC Day 1 (Fig. 7a). This simulated CI location was consistent with the most evident hotspot of CI occurrence during the warm season from 2013 to 2019 (Bai et al. 2020 and Fig. 1b therein), which implied the generality of the control simulation. Initial convective cells gradually developed into a quasi-linear MCS along the coastline in the following 4 h (Figs. 7b,c). There were discrete strong convective elements within the coastal convective rainband similar to observations, but the simulated stratiform rainband to the north was slightly weaker than observed (Fig. 7d and Figs. 2b,d,f), which could possibly be due to the application of a single moment micro-physics scheme (Morrison et al. 2009). The simulated MCS was quite steady over the coastal region and moved eastward

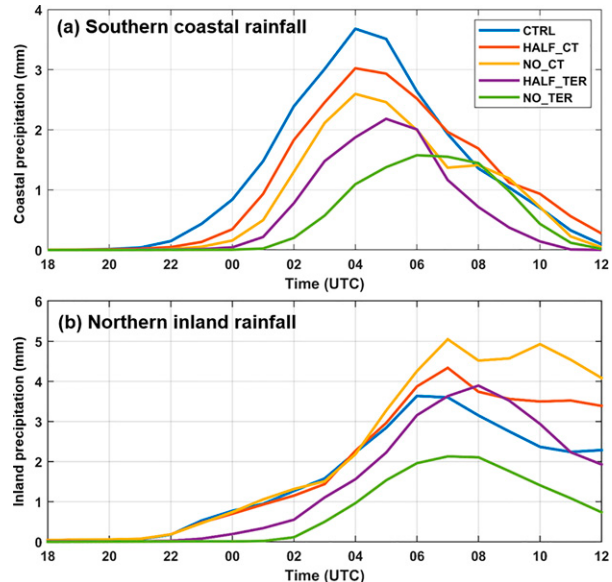


FIG. 8. Time series of hourly area-averaged precipitation over (a) the southern coastal region (the solid box in Fig. 6a) and (b) the northern inland rainfall (the dashed box in Fig. 6a) in CTRL and different sensitivity experiments, with colors corresponding to different experiments as shown in the top-right box in (a).

slowly from 0100 to 0500 UTC Day 2 with continuous back-building on the western end (Figs. 7e,f). The simulated coastal MCS was sustained for more than 10 h and started to dissipate at ~0700 UTC Day 2. It must be noted that there were convective systems developing over the inland region after 0300 UTC Day 2 (Figs. 7e–h) that were not observed in the selected cases. However, considering the similarities in the initiation and organization of the coastal MCS and associated rainfall distribution between CTRL and observations, we believe that this quasi-idealized simulation can be used to investigate mechanisms for the warm-sector heavy-rain-producing MCSs over the coastal region and its response to changes in topography.

4. Responses of heavy rainfall and MCS to terrain changes

The southern coastal terrain, though with relatively small altitude (~500 m), exerted a vital influence on the rainfall distribution over the coastal and inland region, as well as on the location and magnitude of the rainfall maximum. Based on CTRL, four terrain-modification sensitivity experiments were performed (Table 2). The 12-h accumulated rainfall intensities and distributions varied significantly with different terrain changes (Fig. 6). When the southern coastal terrain was reduced (CTRL, HALF_CT, and NO_CT), the coastal heavy rainfall significantly lessened (Figs. 6a–c), with the rainfall maximum decreasing from 345.9 to 185.9 mm (~46% less). This indicates that the existence of the coastal terrain almost doubled the maximum rainfall accumulations associated with the warm-sector heavy rainfall, even though

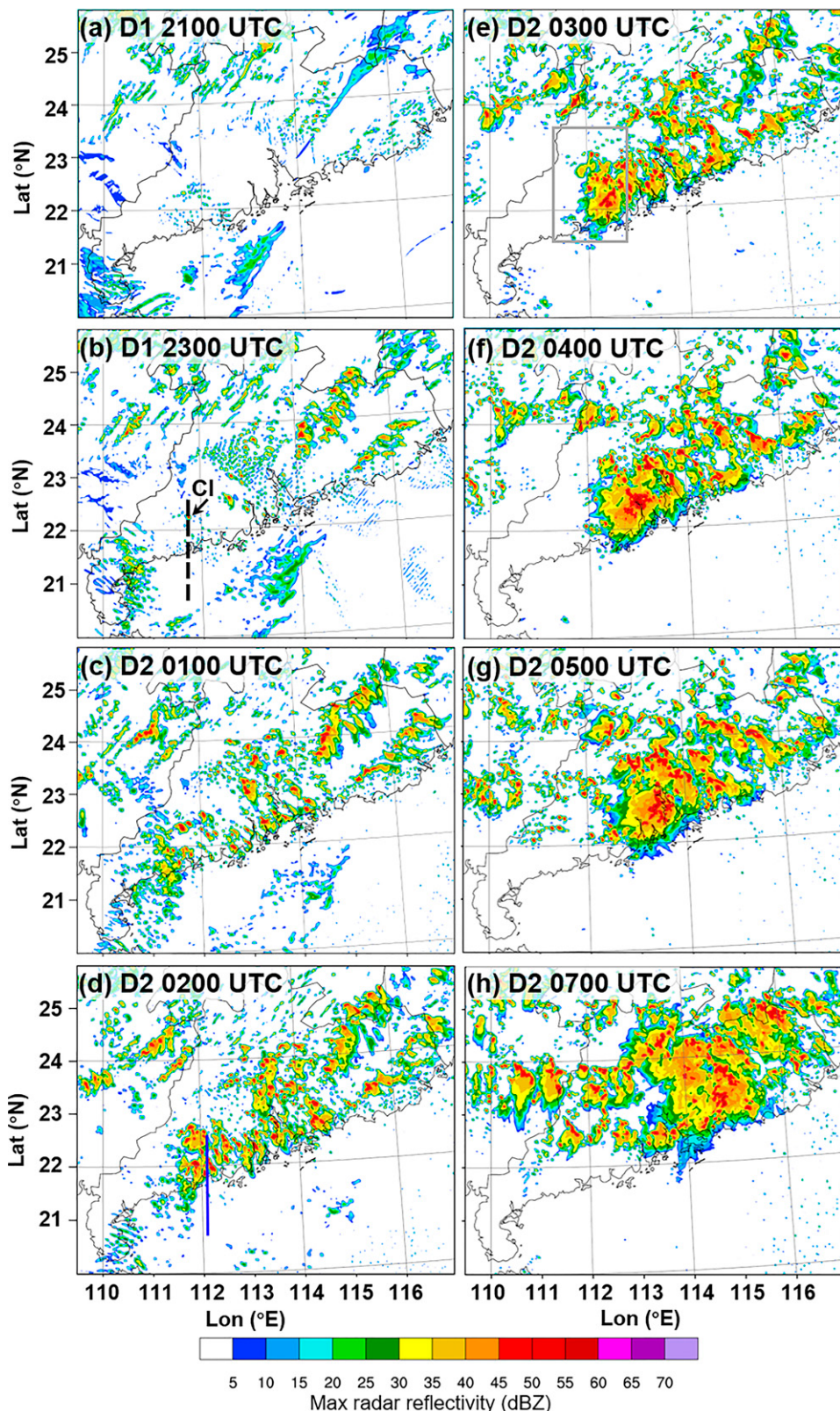


FIG. 9. As in Fig. 7, but for NO_CT. The locations of the black dashed line, the blue line and the gray box are as those in Fig. 7.

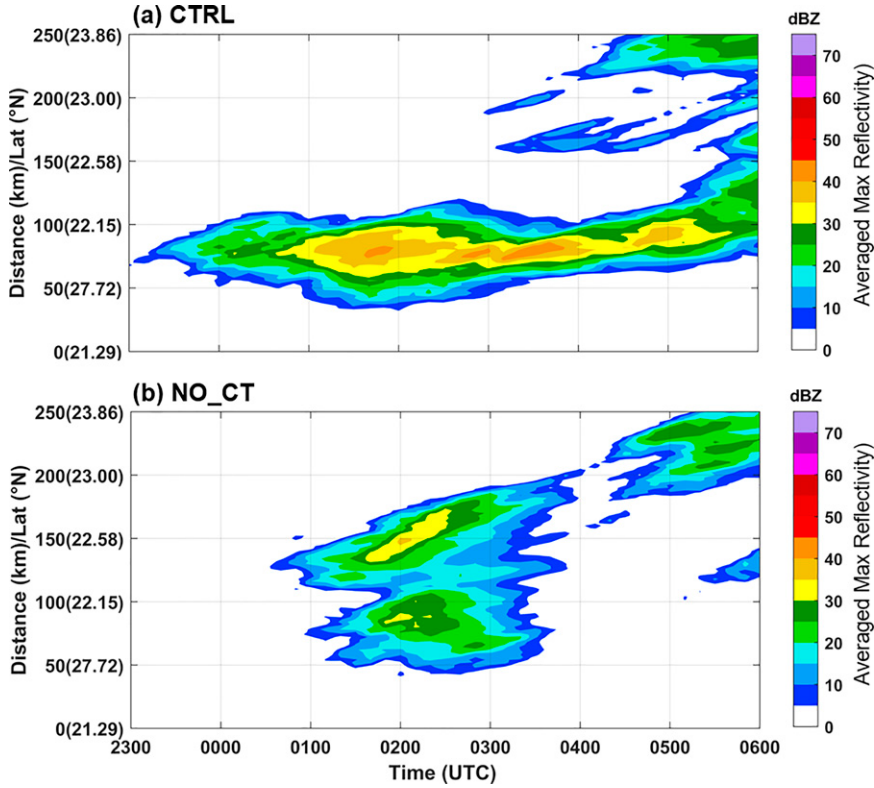


FIG. 10. Time–distance (Hovmöller) diagram of the maximum reflectivity (shading; dBZ) averaged in west–east orientation within the gray box shown in Fig. 7e as well as in Fig. 9e in (a) CTRL and (b) NO_CT.

the coastal terrain height is much lower than other topography in the domain (Fig. 1). Notably, the location of the coastal rainfall maximum shifted eastward with decreasing terrain height, indicating the weakening of back-building processes on the western end of the MCS. The inland rainfall, however, became more widespread and merged with the coastal rainfall (Figs. 6a–c). As the terrain height over the entire domain was reduced in HALF_TER and NO_TER, the 12-h accumulated precipitation was gradually reduced in both coastal and inland regions (Figs. 6d,e) compared with CTRL. These results show that the southern coastal terrain plays an important role in enhancing coastal rainfall maxima.

The hourly rainfall time series quantitatively revealed the rainfall difference among the five experiments (Fig. 8). Over the southern coastal region, the initiation of the precipitation system was delayed with smaller hourly rainfall intensity as the coastal terrain height is reduced (CTRL, HALF_CT and NO_CT; Fig. 8a), indicating a weaker MCS with later CI. The area-averaged rainfall over the northern inland region started to differ in the later stages of the MCS development (after 0400 UTC Day 2), and the rainfall intensity increased with decreasing coastal terrain (Fig. 8b), which was corroborated with more widespread inland rainfall shown in Figs. 6a–c. Compared with the monotonic influence of the southern coastal terrain, the influences of the terrain changes over the whole domain were less regular (Fig. 8). Although the hourly

precipitation over both the southern coastal and northern inland regions generally decreased from 2200 UTC Day 1 to 0700 UTC Day 2 as the terrain height over the entire domain was reduced, the hourly precipitation over the northern inland region in HALF_TER became greater than CTRL after 0700 UTC. Since the precipitation monotonically responded to the linear reduction of southern coastal terrain, the differences between CTRL and NO_CT will be the main focus for the rest of the current study.

The initiation and organization of the heavy-rain-producing MCS were also greatly influenced by the coastal terrain. The major differences of the MCS development between CTRL and NO_CT (Figs. 7 and 9) can be summarized as follows:

- 1) The MCS in CTRL initiated earlier near the coast and the CI location was more to the south compared with that in NO_CT. The CI timing was 2100 UTC Day 1 in CTRL (Fig. 7a) while 2300 UTC Day 2 in NO_CT (Fig. 9b). This is consistent with the delayed increase in rainfall with decreasing terrain height in the hourly rainfall time series of CTRL, HALF_CT and NO_CT shown in Fig. 8a.
- 2) The MCS in CTRL was more organized with a quasi-linear structure and was concentrated in the coastal region. On the contrary, in NO_CT the MCS was less organized and more widespread over the inland region (Figs. 7c,d and Figs. 9d,e), although the convection intensity was comparable with that of CTRL.

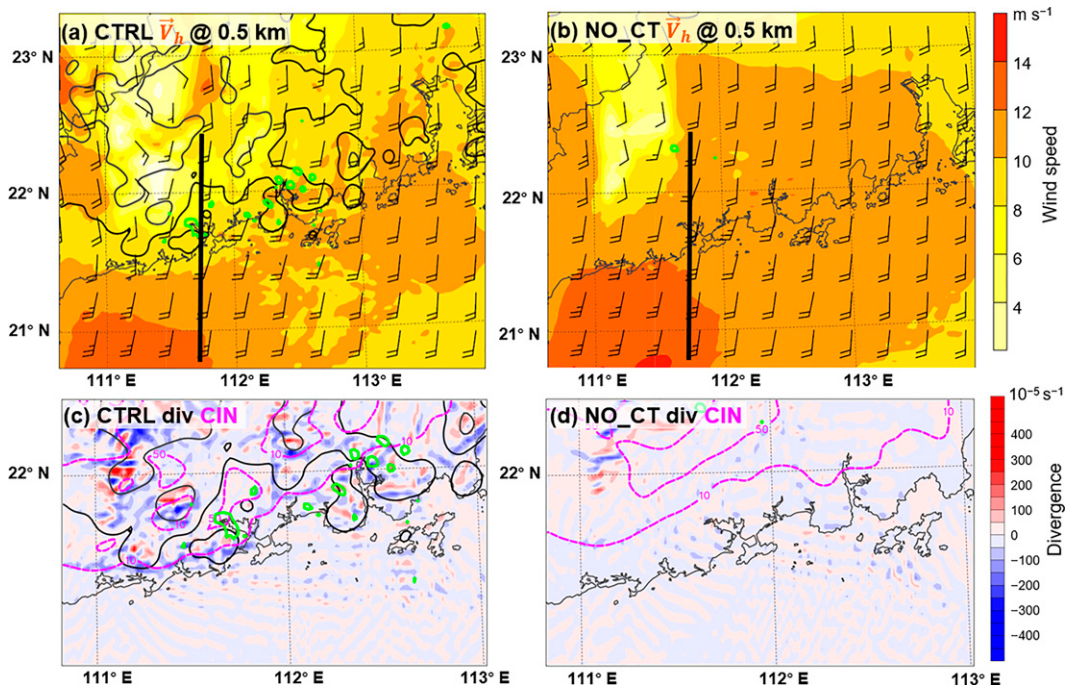


FIG. 11. Wind fields within the boundary layer at 2100 UTC Day 1 (~CI timing in CTRL). (a),(b) Horizontal wind speed (shading; m s^{-1}) and wind vector (full barb denotes 5 m s^{-1} , half barb denotes 2.5 m s^{-1}) at 0.5 km AGL in CTRL and NO_CT, respectively. Also shown are horizontal divergence (shading; 10^{-5} s^{-1}) at the bottom model level and surface-based CIN (contoured in dashed magenta; J kg^{-1}) in (c) CTRL and (d) NO_CT. The terrain height of 300 and 50 m is contoured in gray and black, respectively. The simulated maximum radar reflectivity of 35 dBZ is contoured in green. The thick black line in (a) and (b) denotes the path for the vertical cross sections in Fig. 12, of which the location is the same as in Figs. 7a and 9b.

- 3) There were stronger back-building processes on the western side of the MCS in CTRL compared with NO_CT (Figs. 7e,f and 9e,f). The Hovmöller diagrams of reflectivity between CTRL and NO_CT clearly quantify the differences in back-building (Fig. 10). In CTRL, there was persistent strong convection on the western flank of the quasi-linear MCS resulting from the strong back-building process, sustaining for ~ 5 h. In contrast, the convection on the western flank of the MCS in NO_CT was weaker with a sustaining period of ~ 2 h, indicating a weaker back-building process when the coastal terrain was absent. The stronger back-building process in CTRL was responsible for a larger rainfall maximum located further west (Figs. 6a,c).

In the following section, the reasons behind the differences in the CI and organization mentioned above will be investigated to elucidate the influence of the coastal terrain on the warm-sector heavy-rain-producing MCS evolution.

5. Coastal terrain influence on the initiation and organization of the MCS

a. Convection initiation

The small coastal terrain over southern Guangdong greatly facilitated the CI process by modifying the wind field within the boundary layer and providing strong coastal convergence.

In NO_CT, the horizontal wind speed at 0.5 km AGL (~the height of BLJ) over the coastal region was $\sim 2 \text{ m s}^{-1}$ larger than that in CTRL (Figs. 11a,b), showing a stronger BLJ intruding into the northern inland region and a weaker wind speed gradient near the coast. In contrast, the wind speed in CTRL declined significantly due to the orographic blocking effects of the coastal terrain, leading to a high wind speed gradient near the southern coast (BLJ terminus). As a result, there was strong coastal convergence near the surface that provided favorable conditions for CI in CTRL (Fig. 11c), which was nearly absent in NO_CT at 2100 UTC Day 1 (Fig. 11d). The surface-based CINs over the coastal region in both experiments were comparable and relatively small with a magnitude of $\sim 0\text{--}50 \text{ J kg}^{-1}$ (Figs. 11c,d). The magnitude of CIN in CTRL was $\sim 10 \text{ J kg}^{-1}$ greater over the coastal region, which might have partly helped in the accumulation of CAPE.

The vertical cross section near the CI location further revealed the impact of the coastal terrain on CI processes. In CTRL, the core of the BLJ was weaker and located further south, and the initial convection appeared when the periphery of the BLJ impinged on the coastal terrain (Fig. 12a). However, in NO_CT, the BLJ strongly intruded into the inland region (Fig. 12b), with the strong convergence located further north associated with the BLJ terminus (Fig. 12d) that eventually led to the initial convection further inland ($\sim 75 \text{ km}$

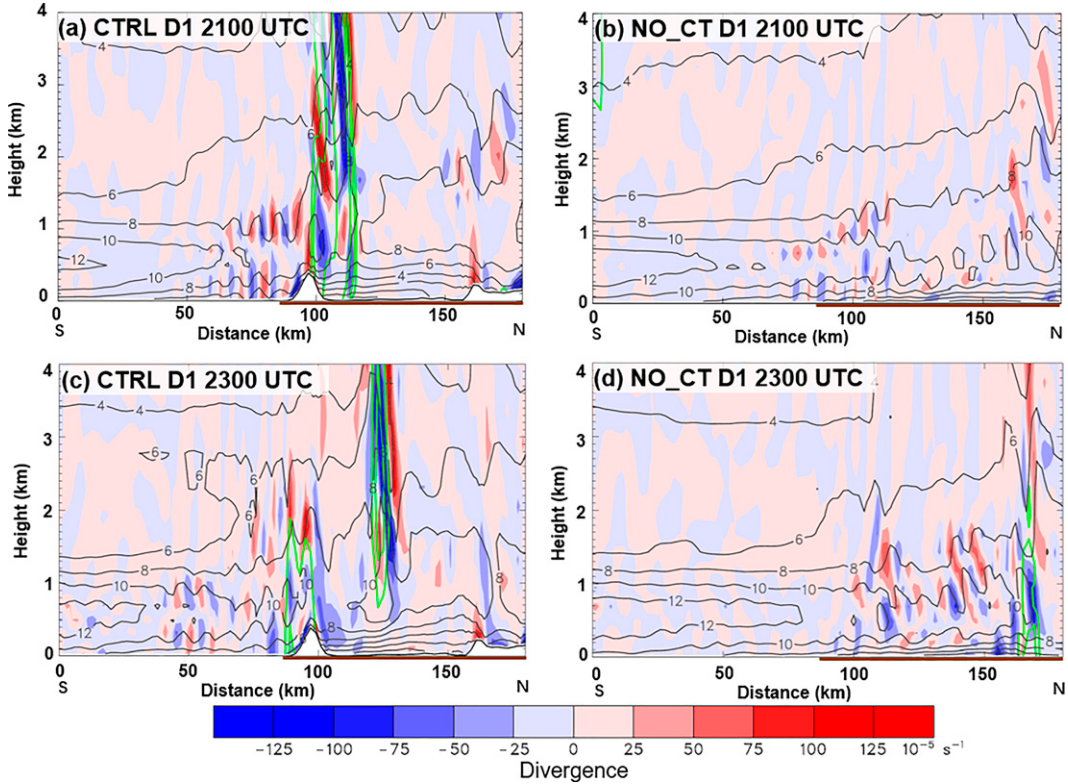


FIG. 12. Vertical north–south cross sections (path given in Figs. 7a, 9b) of horizontal divergence (shading; 10^{-5} s^{-1}), horizontal wind speed along the cross section (contoured in black every 2 m s^{-1}), and simulated radar reflectivity (contoured in green every 10 dBZ over 15 dBZ) at 2100 and 2300 UTC of (a),(c) CTRL and (b),(d) NO_CT. The brown bold line denotes the land area of the cross section. The variables plotted here were averaged over the zone of 4 km perpendicular to and centered at the path.

away from the coast) compared with that in CTRL. The inland movement of CI location with the removal of the coastal terrain in the present study is notably different from the results in Du et al. (2020). In their terrain sensitivity experiments, the CI location shifted southward from the coastal hills to the coastline after removing the coastal terrain because the horizontal convergence associated with the land–sea friction contrast became prominent without the orographic lifting associated with flow interaction with the coastal hills. Nevertheless, in NO_CT, the horizontal convergence associated with the BLJ terminus was stronger than that along the coastline (Fig. 12d), and therefore resulted in CI further inland.

In addition to the influence on CI location, the coastal terrain also advanced the CI timing due to the early existence of coastal convergence. As mentioned in section 4, the CI timing in CTRL was ~2 h earlier than in NO_CT (Figs. 7 and 9). The BLJ in both experiments translated northward and the near-surface wind speed over the coastal region increased with time (Fig. 13). Moreover, the high wind speed core (larger than 10 m s^{-1}) and its related strong convergence moved northward near the coast (~90 km) at approximately the same time (~0000 UTC Day 2) in both experiments (Fig. 13). However, there had been considerable coastal convergence in

CTRL since 2000 UTC Day 1 as the northern periphery of the BLJ impinged on the costal terrain, which was beneficial for the earlier CI (Fig. 13a). Without the coastal terrain, the coastal convergence was rather weak in NO_CT (Fig. 13b) until the high wind speed core moved northward into the coastal region at ~0000–0200 UTC Day 2, which brought strong horizontal convergence favorable for the occurrence of initial convection in NO_CT.

b. MCS organization

The coastal terrain also modulated the organization of the MCS and therefore the heavy rainfall distribution by altering the dynamic and thermodynamic environments. In remainder of this section, the differences in the MCS organization between CTRL and NO_CT will be investigated, including the upscale growth of convection and back-building process, and the role of the coastal terrain therein will be revealed.

The upscale growth of convection can be accelerated in environments when the deep-layer wind shear has a large parallel component and a small perpendicular component with respect to the convection-initiating boundary (Markowski and Richardson 2010). Such an environment promotes hydrometers fallout in the along-line direction and thus results in a

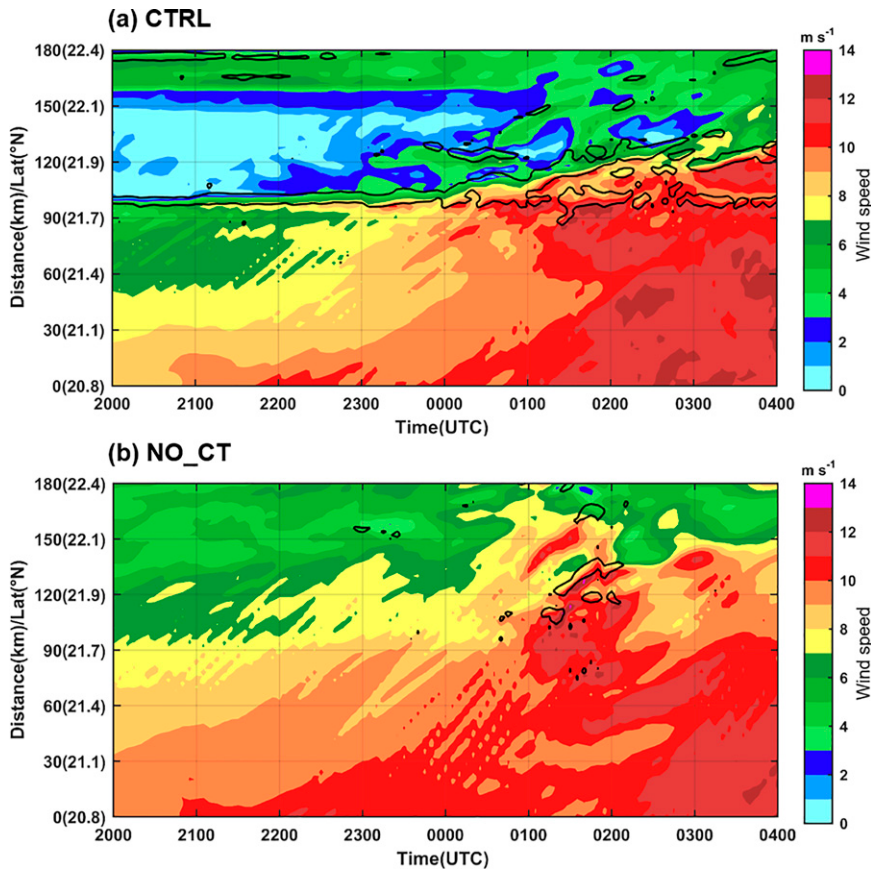


FIG. 13. Time–distance (Hovmöller) diagram of the horizontal wind speed (shading; m s^{-1}) and divergence (black contour of $-8 \times 10^{-4} \text{ s}^{-1}$) at the second model level from the bottom along the path shown in Fig. 7a as well as in Fig. 9b in (a) CTRL and (b) NO_CT. The variables plotted here were averaged over the zone of 4 km perpendicular to and centered at the path.

more rapid transition into a continuous surface gust front and subsequent along-line precipitation (James et al. 2005). Dial et al. (2010) further reinforced that smaller normal components of mean wind with respect to the synoptic initiating boundary can prolong the residence time of storms within the zone of linear forcing along the boundary, thereby increasing the potential for upscale linear growth.

In the current study, the coastline ($\sim 22^\circ$ with respect to the x axis, given in Fig. 14a) can be approximated as the convection-initiating boundary as the orientation of initial convective cells in both CTRL and NO_CT were generally along the coastline. During the early stage after CI in CTRL (Fig. 14a), the 0–6-km vertical wind shear was generally westerly over the land and turned to northwesterly over the ocean, with the magnitude of the component normal to the convection-initiating boundary increasing offshore (Fig. 14c). This was consistent with the 0–6-km vertical wind shear feature in the three cases and their composite fields in FNL analysis (not shown).

The parallel and normal components of deep-layer vertical wind shear and mean wind with respect to the convection-initiating boundary in CTRL and NO_CT at 2 h after CI were further examined. The area-averaged parallel component of

0–6-km vertical wind shear in CTRL was $\sim 0.9 \text{ m s}^{-1}$ larger than that in NO_CT, while the normal component in CTRL was $\sim 2.4 \text{ m s}^{-1}$ smaller than that in NO_CT (Figs. 14a–d). These differences in deep-layer vertical wind shear were likely induced by the smaller near-surface southerly winds in CTRL compared with NO_CT, which eventually favored the faster linear upscale growth of the initial discrete cells in CTRL as shown in Fig. 7. Moreover, the 0–6-km mean wind over the coastal region in CTRL generally decreased by $\sim 0.6 \text{ m s}^{-1}$ due to the weakening of low-level wind associated with the blocking of the coastal terrain compared with NO_CT (Figs. 14e,f). The weaker deep-layer mean wind in CTRL slowed down the onshore movement of the initial convective cells, increased their residence time along the convection-initiating boundary, and accelerated the upscale growth along the coast. Therefore, in addition to directly strengthening the horizontal convergence near the coast as commonly revealed by previous studies over the southern coastal region (e.g., Chen et al. 2017; Bai et al. 2020; Du et al. 2020), the coastal terrain also plays a vital role in fostering the upscale growth of the warm-sector MCSs by modulating the environmental deep-layer vertical wind shear and weakening the deep-layer mean wind.

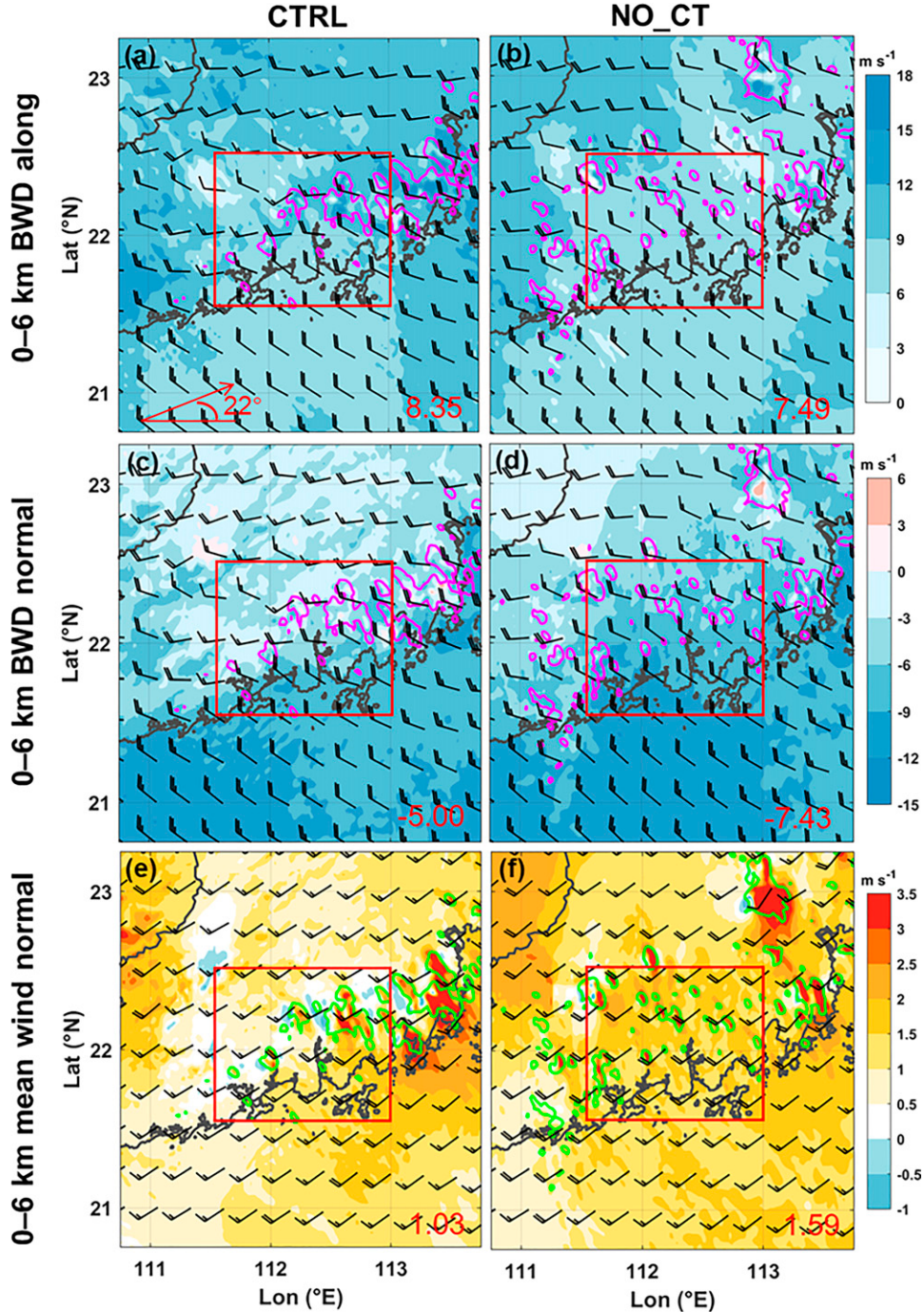


FIG. 14. Plan views of the 0–6-km bulk wind difference (BWD) (full barb denotes 5 m s^{-1} , half barb denotes 2.5 m s^{-1}), 0–6-km BWD component along the convection-initiating boundary (shading; m s^{-1}), and simulated maximum radar reflectivity (magenta contour of 35 dBZ) in (a) CTRL at 2300 UTC Day 1 and (b) NO_CT at 0100 UTC Day 2. (c),(d) As in (a) and (b), but for the 0–6-km BWD component normal to the convection-initiating boundary (shading; m s^{-1}). (e) The plan views of the 0–6-km mean wind normal to the convection-initiating boundary (shading; m s^{-1}), 0–6-km mean wind vector (full barb denotes 5 m s^{-1} , half barb denotes 2.5 m s^{-1}), and simulated maximum radar reflectivity (green contour of 35 dBZ) in CTRL at 2300 UTC Day 1; and (f) as in (e), but the NO_CT at 0100 UTC Day 2. The orientation of the convection-initiating boundary is approximated as along the coast, which is denoted by the red arrow in (a). The area-averaged shading values over the red boxes are given in the bottom right, respectively.

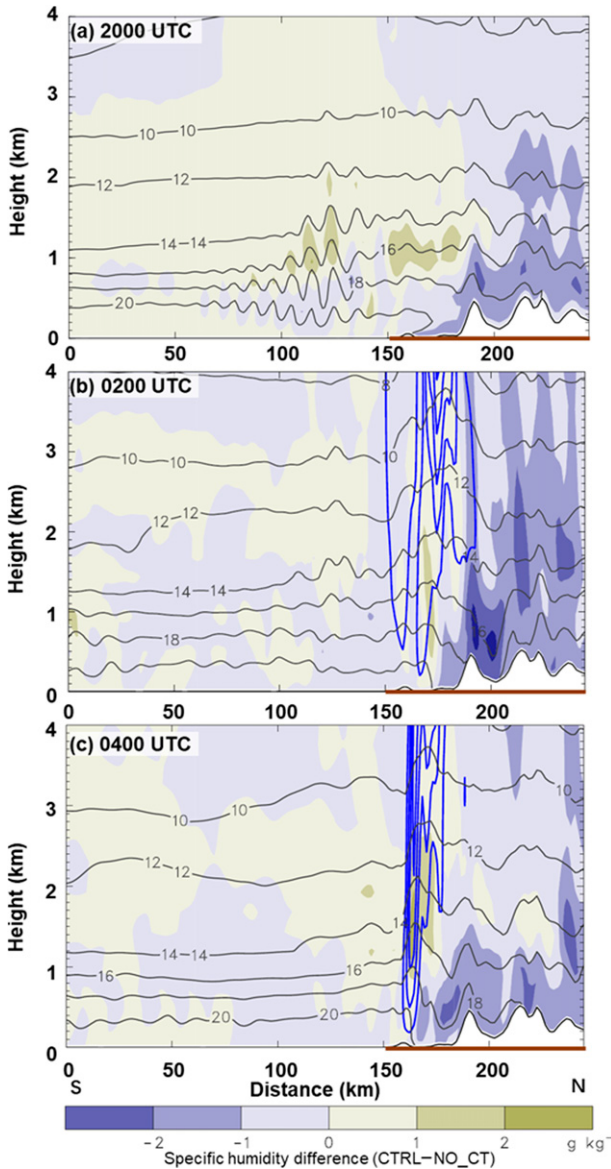


FIG. 15. Vertical north-south cross sections (path given in Fig. 7d as well as in Fig. 9d) of the differences in specific humidity between CTRL and NO_{CT} (CTRL – NO_{CT}) (shading; g kg^{-1}), specific humidity (contoured in black; g kg^{-1}), and vertical velocity in CTRL (contoured in blue every 1 m s^{-1} over 0.5 m s^{-1}) at (a) 2000 UTC Day 1, (b) 0200 UTC Day 2, and (c) 0400 UTC Day 2. The brown bold line denotes the land area. The variables plotted here were averaged over the zone of 20 km perpendicular to and centered at the path.

Notably, Dial et al. (2010) suggested that the cloud-layer (2–6 km) vertical wind shear may be a better discriminator for different convection evolution modes with strong synoptic initiating boundaries. However, due to the strong low-level southerly over the southern coastal region, the 2–6-km vertical wind shear was relatively small (less than 5 m s^{-1}) with slight differences between CTRL and NO_{CT}. This implies that for the warm-sector convective processes with a strong LLJ, the 0–6-km vertical wind shear may play a

more important role than the 2–6-km vertical wind shear in modulating the upscale convective growth of warm-sector MCSs.

The coastal terrain also modulated the distribution of thermodynamic fields, such as moisture and instability, and eventually led to a quasi-linear MCS concentrated over the coastal region. In CTRL, the moisture under 2 km AGL over the inland region was at least 1 g kg^{-1} smaller than that in NO_{CT} (Fig. 15), which was likely due to weaker horizontal wind speeds and associated moisture transport within the boundary layer. The drier air contributed to a smaller CAPE over the inland region in CTRL, which resulted in strong convective updrafts concentrated over the coastal region (Figs. 16a,c,e). Notably, there was smaller moisture and CAPE over the inland region in CTRL compared with NO_{CT} at 2000 UTC Day 1 (Figs. 15a and 16a,b), suggesting that the differences had already been induced by the modification in the coastal terrain before the CI. In contrast, in NO_{CT} the inland moisture was higher due to the stronger BLJ, which eventually led to higher inland CAPE with an increment of $\sim 1000\text{--}2000 \text{ J kg}^{-1}$ compared with CTRL. Consequently, the strong convective updrafts were widespread over both the coastal and inland regions in NO_{CT} as shown in the cross section at 0200 UTC Day 2 (Fig. 16d), but moved rapidly out of the cross section at 0400 UTC due to the faster propagation of the MCS in NO_{CT} (Fig. 16f).

Back-building processes were essential in the heavy-rain-producing MCS and were facilitated by the small coastal terrain through cold pool interactions. In CTRL, new convective cells were persistently generated on the western end of the MCS at $\sim 0200\text{--}0300 \text{ UTC Day 2}$ (Figs. 17a–c), gradually merging with the parent storm to the east (Fig. 17d). Both the small coastal terrain lifting and the strong and stagnant cold pool outflow boundary were favorable for the generation of new cells (Fig. 17b). The cold pool in CTRL was fixed in place near the windward slope although the parent storm was moving northeastward (Figs. 17e,f), similar to the stationary cold pool features induced by high terrain over central Taiwan in Xu et al. (2012). This implies that the coastal terrain is still capable of “trapping” the cold pool like a small “cold air damming,” despite having relatively small terrain heights of $\sim 500 \text{ m}$. The convergence and lifting near the edge of the stagnant cold pool (Fig. 17f, $\sim 30 \text{ km}$) led to persistent generation of new cells. In contrast, the cold pool in NO_{CT} was weaker with an ambiguous outflow boundary (Figs. 18a–d) and moved northeastward quickly without being blocked by the coastal terrain (Figs. 18e,f), which was detrimental for the back-building process. The stronger cold pool in CTRL could be attributed to the blocking of the coastal terrain, and was also favored by the subsequent positive feedbacks between precipitation and cold pools.

6. Summary

This study investigated the general impacts of small coastal terrain on warm-sector heavy-rain-producing MCSs in southern China using quasi-idealized WRF simulations and terrain-modification experiments. Three warm-sector heavy rainfall

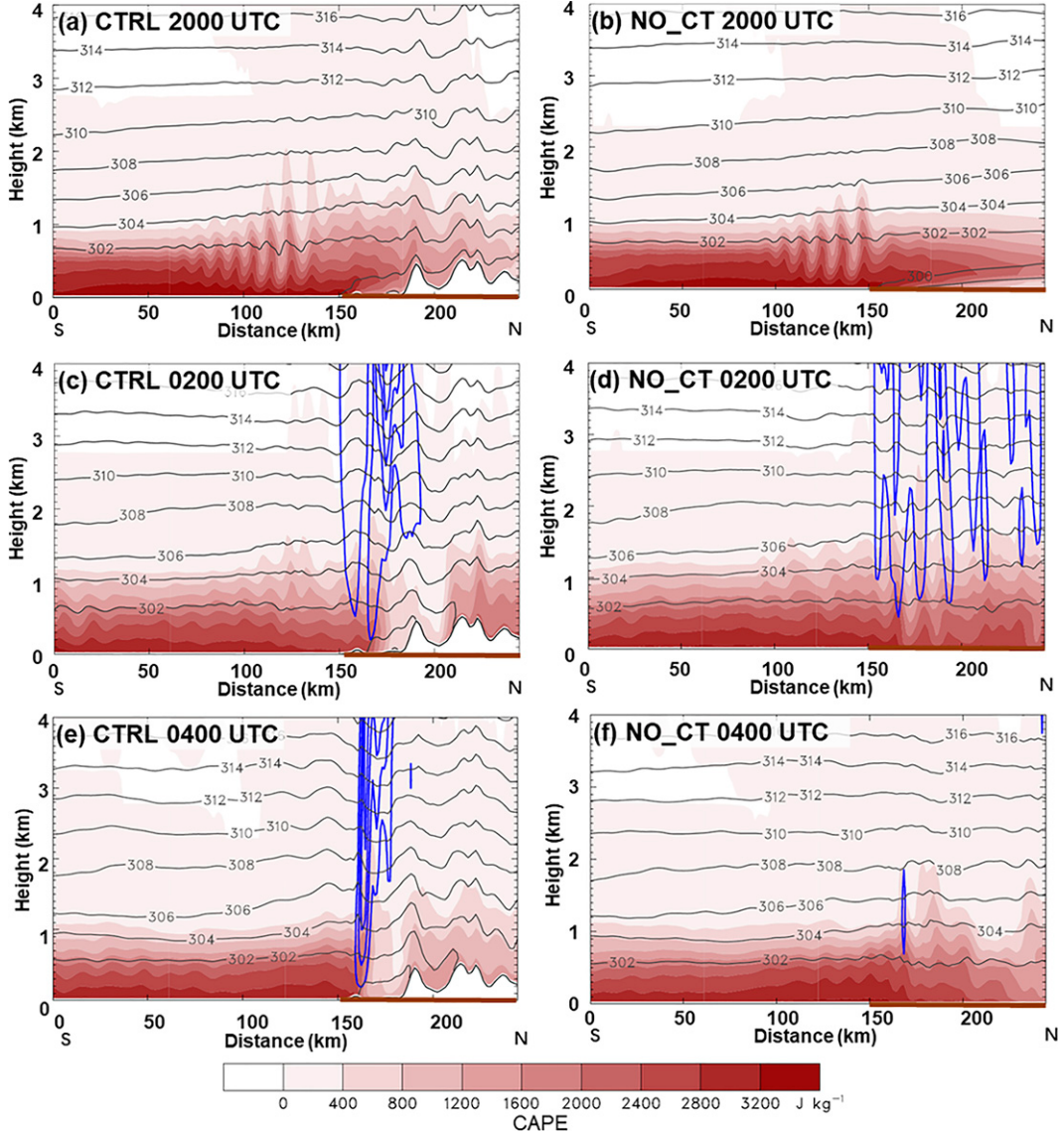


FIG. 16. Vertical north–south cross sections (path given in Fig. 7d as well as in Fig. 9d) of CAPE (shading; $J \text{ kg}^{-1}$), potential temperature (contoured in black; K), and vertical velocity (contoured in blue every 1 m s^{-1} over 0.5 m s^{-1}) in CTRL at (a) 2000 UTC Day 1, (c) 0200 UTC Day 2, and (e) 0400 UTC Day 2. (b),(d),(f) As in (a), (c), and (e), but for NO_CT. The brown bold line denotes the land area. The variables plotted here were averaged over the zone of 20 km perpendicular to and centered at the path.

events over the southern coast of China from 2013 to 2015 with similar synoptic conditions, MCS life cycle, and precipitation distribution were selected in this study. All of the three MCSs initiated in the early morning, gradually developed into a quasi-linear convective system along the coast, and moved eastward slowly with back-building processes on the western end of the MCS, which was favorable for the accumulation of heavy rainfall.

To understand more generally how small coastal terrain influences the warm-sector heavy-rain-producing MCSs in southern China, quasi-idealized WRF simulations were performed by compositing the atmospheric conditions of the three cases as the initial and boundary conditions for the model integration. The

control simulation reasonably reproduced the life cycle and essential features of the observed MCSs and associated heavy rainfall. By modifying the terrain elevation over the coastal region and the entire domain, results showed that the southern coastal terrain ($\sim 500 \text{ m}$) played an important role in enhancing rainfall maxima, despite being much lower than other topography in the domain. The existence of small coastal terrain features approximately doubled the maximum rainfall (from 185.9 mm in NO_CT to 345.9 mm in CTRL). As the southern coastal terrain was linearly reduced, the inland rainfall was enhanced while the coastal rainfall was weakened. Moreover, the location of the rainfall maximum shifted eastward with decreasing coastal

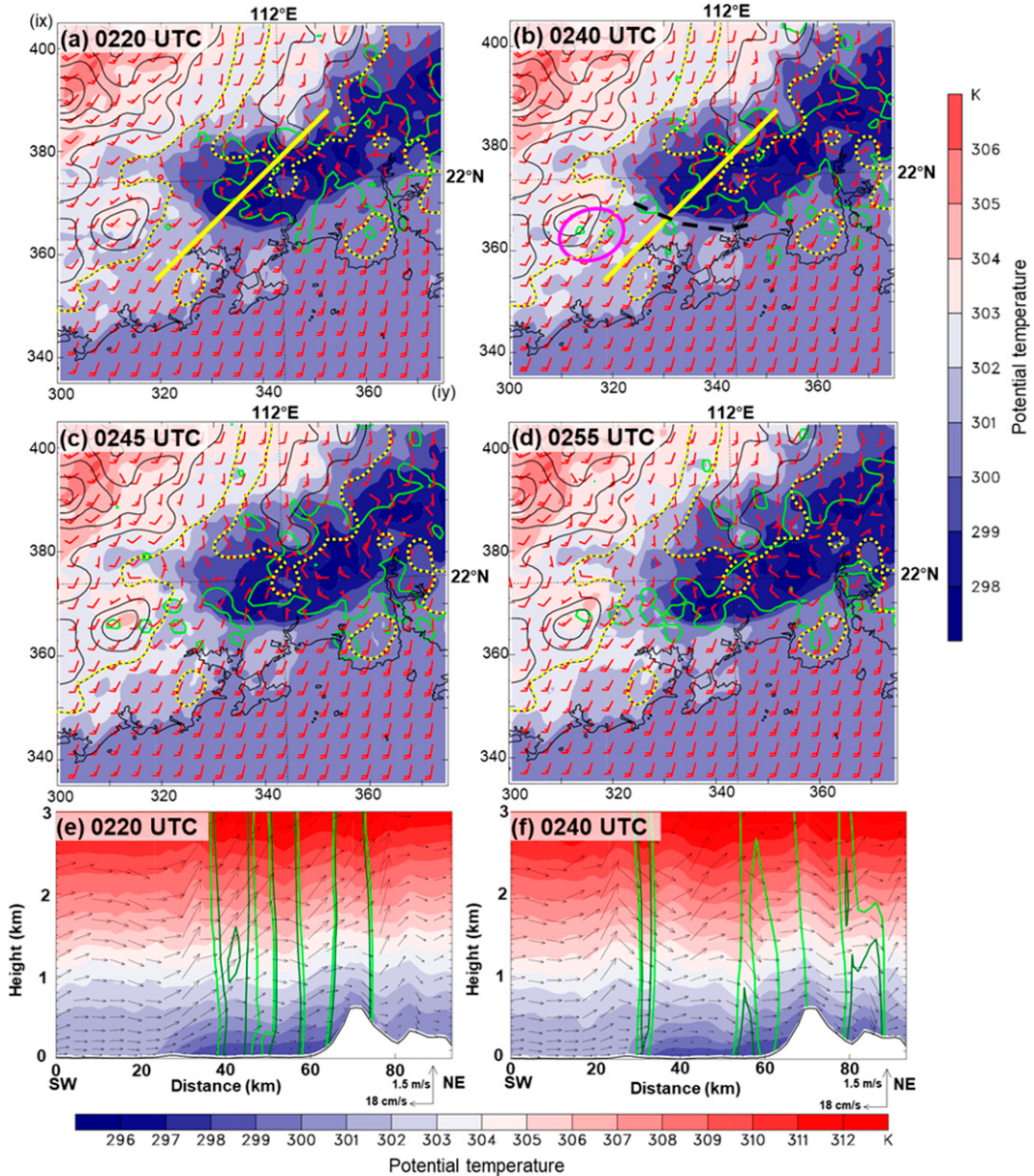


FIG. 17. Potential temperature (shading; K), horizontal wind vector (full barb denotes 5 m s^{-1} , half barb denotes 2.5 m s^{-1}) at the bottom model level, terrain height (contoured in black, every 200 m over 100 m with the 100-m contour highlighted in yellow dotted), and 35-dBZ maximum radar reflectivity (green contour) in CTRL at (a) 0220, (b) 0240, (c) 0245, and (d) 0255 UTC Day 2. The dashed black line in (b) denotes the edge of the cold pool and the magenta circle in (b) denotes the convective cells initiated by small terrain. (e),(f) The vertical cross sections along the yellow path given in (a) and (b), with potential temperature (shading; K), in-plane wind vectors along the cross section (black arrow; reference vector given in the bottom right), and simulated radar reflectivity (dark green contour for 40 dBZ, light green for 35 dBZ).

terrain, largely due to the lack of back-building processes with lower topography.

The impacts of the coastal terrain on warm-sector heavy-rain-producing MCSs can be schematically summarized in Fig. 19. Due to the blocking effects of the coastal terrain, there is a weaker BLJ with a stronger horizontal wind speed gradient and convergence near the coast in CTRL compared

with NO_CT. The convection initiates ~ 2 h earlier as the northern periphery of the BLJ impinges on the coastal terrain in the early morning. In addition to the influence on CI, the coastal terrain can also modify the organization of the MCS and therefore the precipitation distribution through altering the dynamic and thermodynamic environments. The weaker near-surface winds due to the friction of the coastal terrain

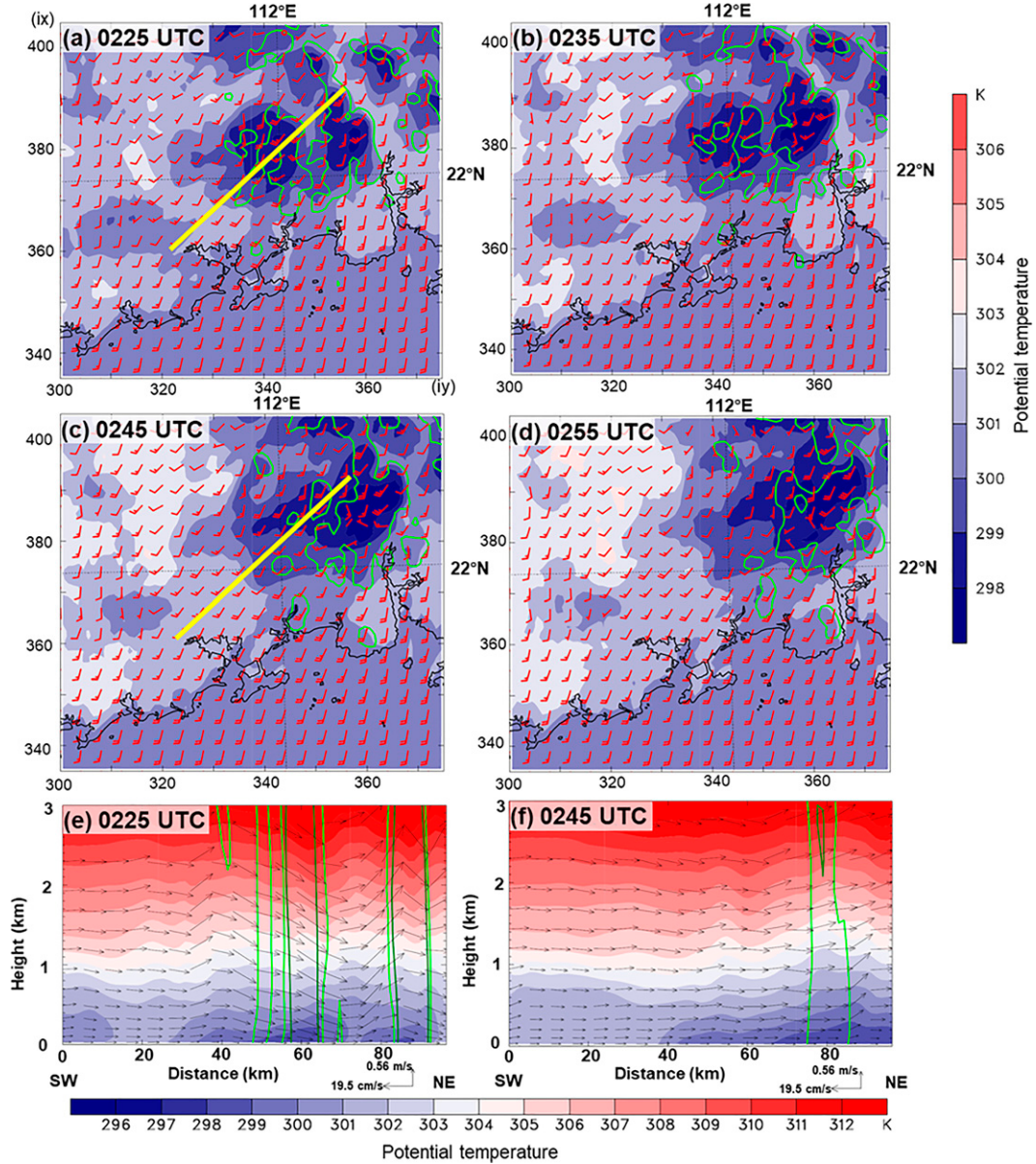


FIG. 18. As in Fig. 17, but for NO_CT at (a) 0225, (b) 0235, (c) 0245, (d) 0255, (e) 0225, and (f) 0245 UTC Day 2.

result in a smaller 0–6-km vertical wind shear component perpendicular to the coast and a larger component parallel to the coast. The environmental 0–6-km mean wind is also weakened by the coastal terrain. These modifications in dynamic environments are favorable for the initial convective cells to grow upscale into an organized quasi-linear structure more rapidly. Moreover, the weaker BLJ also results in decreased moisture transport into the inland region and therefore smaller CAPE. As a result, the MCS is more likely to be concentrated in the coastal region rather than develop into widespread convection over the inland region. The coastal terrain, despite its relatively small heights, is still capable of trapping the cold pool and facilitating a small “cold air damming” effect. The stagnant cold pool favors the persistent generation

of new cells on the western side of the MCS, which is essential for the formation of heavy rainfall.

The current study provides a relatively general picture of how the coastal terrain with small heights influences the evolution of deep convective systems during the warm-sector heavy rainfall over southern China. By modulating low-level winds, the thermodynamic fields including moisture and instability, and features of cold pools, the coastal terrain fosters a more organized and persistent MCS with an early initiation, which poses a greater threat of flooding over this high-populated region. Conclusions drawn here might also be indicative in understanding the role of small hills in the development of the MCSs over other coastal areas around the world, especially when warm and moist oceanic

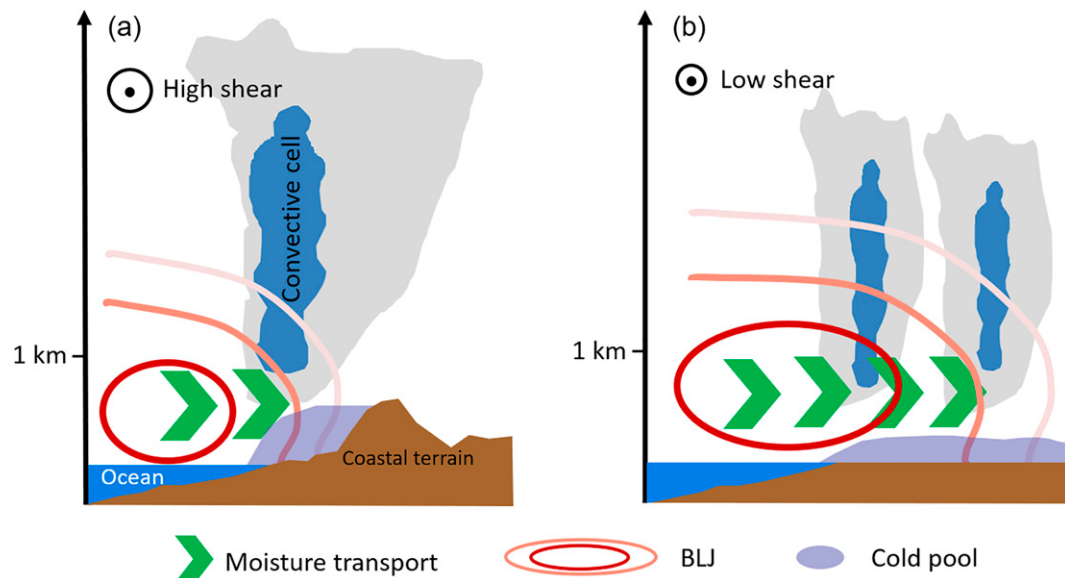


FIG. 19. Schematic diagram of the impacts of coastal terrain on warm-sector heavy-rain-producing MCSs. BLJ (red contour), moisture transport (green arrow), cold pool (light purple blob), environmental vertical wind shear (denoted on the top left) conditions, and convective cells (shading clusters) in (a) CTRL and (b) NO_CT.

airflows impinge on the coast in a weakly forced synoptic environment.

Acknowledgments. This work was sponsored by the National Natural Science Foundation of China (Grants 42030604, 41875051, and 41905049), NSF Grant AGS-1854399, Graduate School of Peking University (Visiting Student Scholarship in 2019), and China Postdoctoral Science Foundation (Grant 2021M702725). Dr. Murong Zhang is also sponsored by the MEL Outstanding Postdoctoral Scholarship from Xiamen University. The authors thank Prof. Russ S. Schumacher at Colorado State University for many thought-provoking discussions with him on this work.

REFERENCES

- Bai, L., G. Chen, and L. Huang, 2020: Convection initiation in monsoon coastal areas (South China). *Geophys. Res. Lett.*, **47**, e2020GL087035, <https://doi.org/10.1029/2020GL087035>.
- , —, Y. Huang, and Z. Meng, 2021: Convection initiation at a coastal rainfall hotspot in South China: Synoptic patterns and orographic effects. *J. Geophys. Res. Atmos.*, **126**, e2021JD034642, <https://doi.org/10.1029/2021JD034642>.
- Chen, X., F. Zhang, and K. Zhao, 2016: Diurnal variations of the land-sea breeze and its related precipitation over South China. *J. Atmos. Sci.*, **73**, 4793–4815, <https://doi.org/10.1175/JAS-D-16-0106.1>.
- , —, and —, 2017: Influence of monsoonal wind speed and moisture content on intensity and diurnal variations of the mei-yu season coastal rainfall over South China. *J. Atmos. Sci.*, **74**, 2835–2856, <https://doi.org/10.1175/JAS-D-17-0081.1>.
- Chen, Y.-L., and J. Li, 1995: Large-scale conditions favorable for the development of heavy rainfall during TAMEX IOP 3. *Mon. Wea. Rev.*, **123**, 2978–3002, [https://doi.org/10.1175/1520-0493\(1995\)123<2978:LSCFFT>2.0.CO;2](https://doi.org/10.1175/1520-0493(1995)123<2978:LSCFFT>2.0.CO;2).
- Chu, C.-M., and Y.-L. Lin, 2000: Effects of orography on the generation and propagation of mesoscale convective systems in a two-dimensional conditionally unstable flow. *J. Atmos. Sci.*, **57**, 3817–3837, [https://doi.org/10.1175/1520-0469\(2001\)057<3817:EOOOTG>2.0.CO;2](https://doi.org/10.1175/1520-0469(2001)057<3817:EOOOTG>2.0.CO;2).
- Dial, G. L., J. P. Racy, and R. L. Thompson, 2010: Short-term convective mode evolution along synoptic boundaries. *Wea. Forecasting*, **25**, 1430–1446, <https://doi.org/10.1175/2010WAF2222315.1>.
- Du, Y., and G. Chen, 2019: Heavy rainfall associated with double low-level jets over southern China. Part II: Convection initiation. *Mon. Wea. Rev.*, **147**, 543–565, <https://doi.org/10.1175/MWR-D-18-0102.1>.
- , —, B. Han, L. Bai, and M. Li, 2020: Convection initiation and growth at the coast of South China. Part II: Effects of the terrain, coastline, and cold pools. *Mon. Wea. Rev.*, **148**, 3871–3892, <https://doi.org/10.1175/MWR-D-20-0090.1>.
- Dudhia, J., 1989: Numerical study of convection observed during the Winter Monsoon Experiment using a mesoscale two-dimensional model. *J. Atmos. Sci.*, **46**, 3077–3107, [https://doi.org/10.1175/1520-0469\(1989\)046<3077:NSOCOD>2.0.CO;2](https://doi.org/10.1175/1520-0469(1989)046<3077:NSOCOD>2.0.CO;2).
- He, Z., Q. Zhang, L. Bai, and Z. Meng, 2017: Characteristics of mesoscale convective systems in central East China and their reliance on atmospheric circulation patterns. *Int. J. Climatol.*, **37**, 3276–3290, <https://doi.org/10.1002/joc.4917>.
- Hong, S.-Y., J. Dudhia, and S.-H. Chen, 2004: A revised approach to ice microphysical processes for the bulk parameterization of clouds and precipitation. *Mon. Wea. Rev.*, **132**, 103–120, [https://doi.org/10.1175/1520-0493\(2004\)132<0103:ARATIM>2.0.CO;2](https://doi.org/10.1175/1520-0493(2004)132<0103:ARATIM>2.0.CO;2).
- , Y. Noh, and J. Dudhia, 2006: A new vertical diffusion package with an explicit treatment of entrainment processes. *Mon. Wea. Rev.*, **134**, 2318–2341, <https://doi.org/10.1175/MWR3199.1>.

- Houze, R. A., 2012: Orographic effects on precipitating clouds. *Rev. Geophys.*, **50**, RG1001, <https://doi.org/10.1029/2011RG000365>.
- , Jr. and Coauthors, 2017: The Olympic Mountains Experiment (OLYMPEX). *Bull. Amer. Meteor. Soc.*, **98**, 2167–2188, <https://doi.org/10.1175/BAMS-D-16-0182.1>.
- Hua, S., X. Xu, and B. Chen, 2020: Influence of multiscale orography on the initiation and maintenance of a precipitating convective system in North China: A case study. *J. Geophys. Res. Atmos.*, **125**, e2019JD031731, <https://doi.org/10.1029/2019JD031731>.
- Huang, S. S., 1986: *Heavy Rainfall over Southern China in the Pre-summer Rainy Season* (in Chinese). Guangdong Science and Technology Press, 244 pp.
- Huang, Y., Z. Meng, J. Li, W. Li, L. Bai, M. Zhang, and X. Wang, 2017: Distribution and variability of satellite-derived signals of isolated convection initiation events over central eastern China. *J. Geophys. Res. Atmos.*, **122**, 11357–11373, <https://doi.org/10.1002/2017JD026946>.
- James, R. P., J. M. Fritsch, and P. M. Markowski, 2005: Environmental distinctions between cellular and slabular convective lines. *Mon. Wea. Rev.*, **133**, 2669–2691, <https://doi.org/10.1175/MWR3002.1>.
- Joyce, R. J., J. E. Janowiak, and P. A. Arkin, 2004: CMORPH: A method that produces global precipitation estimates from passive microwave and infrared data at high spatial and temporal resolution. *J. Hydrometeor.*, **5**, 487–503, [https://doi.org/10.1175/1525-7541\(2004\)005<0487:CAMTPG>2.0.CO;2](https://doi.org/10.1175/1525-7541(2004)005<0487:CAMTPG>2.0.CO;2).
- Kumar, A., R. A. Houze Jr., K. L. Rasmussen, and C. Peters-Lidard, 2014: Simulation of a flash flooding storm at the steep edge of the Himalayas. *J. Hydrometeor.*, **15**, 212–228, <https://doi.org/10.1175/JHM-D-12-0155.1>.
- Lee, W.-C., B. J. D. Jou, C.-R. Chen, and J.-A. Moore, 2009: Overview of SoWMEX/TiMREX. *34th Conf. on Radar Meteorology*, Williamsburg, VA, Amer. Meteor. Soc., 9B.2, http://ams.confex.com/ams/34Radar/techprogram/paper_156254.htm.
- Li, J., and Y.-L. Chen, 1998: Barrier jets during TAMEX. *Mon. Wea. Rev.*, **126**, 959–971, [https://doi.org/10.1175/1520-0493\(1998\)126<0959:BJDT>2.0.CO;2](https://doi.org/10.1175/1520-0493(1998)126<0959:BJDT>2.0.CO;2).
- Li, S., Z. Meng, and N. Wu, 2021: A preliminary study on the organizational modes of mesoscale convective systems associated with warm-sector heavy rainfall in South China. *J. Geophys. Res. Atmos.*, **126**, e2021JD034587, <https://doi.org/10.1029/2021JD034587>.
- Luo, Y., H. Wang, R. Zhang, W. Qian, and Z. Luo, 2013: Comparison of rainfall characteristics and convective properties of monsoon precipitation systems over south China and the Yangtze and Huai River basin. *J. Climate*, **26**, 110–132, <https://doi.org/10.1175/JCLI-D-12-00100.1>.
- , R. Xia, and J. C. L. Chan, 2020: Characteristics, physical mechanisms, and prediction of pre-summer rainfall over South China: Research progress during 2008–2019. *Kisho Shishi. Dai2shu*, **98**, 19–42, <https://doi.org/10.2151/jmsj.2020-002>.
- Markowski, P., and Y. Richardson, 2010: *Mesoscale Meteorology in Midlatitudes*. Wiley-Blackwell, 430 pp.
- Medina, S., R. A. Houze Jr., A. Kumar, and D. Niyogi, 2010: Summer monsoon convection in the Himalayan region: Terrain and land cover effects. *Quart. J. Roy. Meteor. Soc.*, **136**, 593–616, <https://doi.org/10.1002/qj.601>.
- Miglietta, M. M., and R. Rotunno, 2009: Numerical simulations of conditionally unstable flows over a ridge. *J. Atmos. Sci.*, **66**, 1865–1885, <https://doi.org/10.1175/2009JAS2902.1>.
- , and —, 2010: Numerical simulations of low-CAPE flows over a mountain ridge. *J. Atmos. Sci.*, **67**, 2391–2401, <https://doi.org/10.1175/2010JAS3378.1>.
- Mlawer, E. J., S. J. Taubman, P. D. Brown, M. J. Iacono, and S. A. Clough, 1997: Radiative transfer for inhomogeneous atmospheres: RRTM, a validated correlated-k model for the longwave. *J. Geophys. Res.*, **102**, 16663–16682, <https://doi.org/10.1029/97JD00237>.
- Morrison, H., G. Thompson, and V. Tatarki, 2009: Impact of cloud microphysics on the development of trailing stratiform precipitation in a simulated squall line: Comparison of one- and two-moment schemes. *Mon. Wea. Rev.*, **137**, 991–1007, <https://doi.org/10.1175/2008MWR2556.1>.
- Mulholland, J. P., S. W. Nesbitt, R. J. Trapp, K. L. Rasmussen, and P. V. Salio, 2018: Convective storm life cycle and environments near the Sierras de Córdoba, Argentina. *Mon. Wea. Rev.*, **146**, 2541–2557, <https://doi.org/10.1175/MWR-D-18-0081.1>.
- , —, and —, 2019: A case study of terrain influences on upscale convective growth of a supercell. *Mon. Wea. Rev.*, **147**, 4305–4324, <https://doi.org/10.1175/MWR-D-19-0099.1>.
- NCEP, 2000: NCEP FNL operational model global tropospheric analyses, continuing from July 1999. Research Data Archive at the National Center for Atmospheric Research, Computational and Information Systems Laboratory, accessed 15 June 2019, <https://doi.org/10.5065/D6M043C6>.
- Peters, J. M., and R. S. Schumacher, 2015: The simulated structure and evolution of a quasi-idealized warm-season convective system with a training convective line. *J. Atmos. Sci.*, **72**, 1987–2010, <https://doi.org/10.1175/JAS-D-14-0215.1>.
- Rackley, J. A., and J. A. Knox, 2016: A climatology of southern Appalachian cold-air damming. *Wea. Forecasting*, **31**, 419–432, <https://doi.org/10.1175/WAF-D-15-0049.1>.
- Ramage, C. S., 1952: Variation of rainfall over South China through the wet season. *Bull. Amer. Meteor. Soc.*, **33**, 308–311, <https://doi.org/10.1175/1520-0477-33.7.308>.
- Rasmussen, K. L., and R. A. Houze Jr., 2011: Orogenic convection in South America as seen by the TRMM satellite. *Mon. Wea. Rev.*, **139**, 2399–2420, <https://doi.org/10.1175/MWR-D-10-05006.1>.
- , and —, 2016: Convective initiation near the Andes in subtropical South America. *Mon. Wea. Rev.*, **144**, 2351–2374, <https://doi.org/10.1175/MWR-D-15-0058.1>.
- , M. D. Zuluaga, and R. A. Houze Jr., 2014: Severe convection and lightning in subtropical South America. *Geophys. Res. Lett.*, **41**, 7359–7366, <https://doi.org/10.1002/2014GL061767>.
- Richwien, B. A., 1980: The damming effect of the southern Appalachians. *Natl. Wea. Dig.*, **5**(1), 2–12.
- Roberts, R. D., and S. Rutledge, 2003: Nowcasting storm initiation and growth using GOES-8 and WSR-88D data. *Wea. Forecasting*, **18**, 562–584, [https://doi.org/10.1175/1520-0434\(2003\)018<0562:NSIAGU>2.0.CO;2](https://doi.org/10.1175/1520-0434(2003)018<0562:NSIAGU>2.0.CO;2).
- Skamarock, W. C., and Coauthors, 2008: A description of the Advanced Research WRF version 3. NCAR Tech. Note NCAR/TN-475+STR, 113 pp., <https://doi.org/10.5065/D68S4MVH>.
- Smith, R. B., 1979: The influence of mountains on the atmosphere. *Advances in Geophysics*, Vol. 21, Academic Press, 87–230, [https://doi.org/10.1016/S0065-2687\(08\)60262-9](https://doi.org/10.1016/S0065-2687(08)60262-9).
- Sun, J., and S. Zhao, 2002: A study of mesoscale convective systems and its environmental fields during the June 1994 record heavy rainfall in South China. Part II: Effect of physical processes, initial environmental fields and topography on meso- β

- convective system (in Chinese). *Chin. J. Atmos. Sci.*, **26**, 633–646, <https://doi.org/10.3878/j.issn.1006-9895.2002.05.05>.
- Tu, C., Y. Chen, P. Lin, and Y. Du, 2019: Characteristics of the marine boundary layer jet over the South China Sea during the early summer rainy season of Taiwan. *Mon. Wea. Rev.*, **147**, 457–475, <https://doi.org/10.1175/MWR-D-18-0230.1>.
- Wang, H., Y. Luo, and B. Jou, 2014: Initiation, maintenance, and properties of convection in an extreme rainfall event during SCMREX: Observational analysis. *J. Geophys. Res. Atmos.*, **119**, 13 206–13 232, <https://doi.org/10.1002/2014JD022339>.
- Wolyn, P. G., and T. B. McKee, 1994: The mountain-plains circulation east of a 2-km-high north-south barrier. *Mon. Wea. Rev.*, **122**, 1490–1508, [https://doi.org/10.1175/1520-0493\(1994\)122<1490:TMPCCEO>2.0.CO;2](https://doi.org/10.1175/1520-0493(1994)122<1490:TMPCCEO>2.0.CO;2).
- Wu, M., and Y. Luo, 2016: Mesoscale observational analysis of lifting mechanism of a warm-sector convective system producing the maximal daily precipitation in China mainland during pre-summer rainy season of 2015. *J. Meteor. Res.*, **30**, 719–736, <https://doi.org/10.1007/s13351-016-6089-8>.
- Xu, W., E. J. Zipser, Y. Chen, C. Liu, Y. Liou, W. Lee, and B. Jong-Dao Jou, 2012: An orography-associated extreme rainfall event during TiMREX: Initiation, storm evolution, and maintenance. *Mon. Wea. Rev.*, **140**, 2555–2574, <https://doi.org/10.1175/MWR-D-11-00208.1>.
- Yeh, H.-C., and Y.-L. Chen, 1998: Characteristics of the rainfall distribution over Taiwan during TAMEX. *J. Appl. Meteor.*, **37**, 1457–1469, [https://doi.org/10.1175/1520-0450\(1998\)037<1457:CORDOT>2.0.CO;2](https://doi.org/10.1175/1520-0450(1998)037<1457:CORDOT>2.0.CO;2).
- , and —, 2002: The role of offshore convergence on coastal rainfall during TAMEX IOP 3. *Mon. Wea. Rev.*, **130**, 2709–2730, [https://doi.org/10.1175/1520-0493\(2002\)130<2709:TROOCO>2.0.CO;2](https://doi.org/10.1175/1520-0493(2002)130<2709:TROOCO>2.0.CO;2).
- Zhang, M., and Z. Meng, 2019: Warm-sector heavy rainfall in southern China and its WRF simulation evaluation: A low-level-jet perspective. *Mon. Wea. Rev.*, **147**, 4461–4480, <https://doi.org/10.1175/MWR-D-19-0110.1>.
- Zhu, L., Z. Meng, F. Zhang, and P. M. Markowski, 2017: The influence of sea- and land-breeze circulations on the diurnal variability of precipitation over a tropical island. *Atmos. Chem. Phys.*, **17**, 13 213–13 232, <https://doi.org/10.5194/acp-17-13213-2017>.